

## ABSTRACT

Title of Document: INVESTIGATION OF MAGNETIC DOMAIN  
CONFIGURATION AND VORTEX-  
ANTIVORTEX CREATION AND  
ANNIHILATION ON CoFeB PATTERNS

Jin Seock Ma, Master of Science, 2011

Directed By: Professor Romel Del Rosario Gomez  
Department of Electrical and Computer  
Engineering

The characteristics of patterned CoFeB films have attracted much attention for spin configurations and magnetization processes of nanostructured elements in that CoFeB has desirable properties including magnetic softness, large magneto-impedance, high spin polarization, and epitaxial registry with MgO(100). In this experiment, micron-sized CoFeB islands with various thicknesses, deposited by a sputtering process, were investigated in order to study their slow micro-magnetic properties as a function of an externally applied magnetic field as well as their remanent domain configurations.

Magnetic Force Microscopy (MFM) of the array at zero applied field revealed that despite a large variation in CoFeB thickness, the remanent domain configurations could be classified into several unique domain configurations. Selected islands of

dimensions from  $0.25\mu\text{m} \times 0.25\mu\text{m}$  to  $16\mu\text{m} \times 16\mu\text{m}$  were studied using MFM equipment.

In addition, the creation and annihilation of magnetic vortex and antivortex pairs in cross-tie walls on CoFeB islands of  $16\mu\text{m} \times 4\mu\text{m}$  were investigated using MFM in the presence of an applied field. The first vortex-antivortex pair is nucleated in a 4-domain Landau pattern from a section of a 180 degree Néel wall as a consequence of the formation of an end domain closure pattern. The vortex-antivortex pair creation satisfies the condition that the closure domain vortices have the same chiralities. Pair annihilation was found to occur in two steps: a rapid advance of the vortices toward the more or less fixed antivortices followed by a deceleration caused by the decrease in local susceptibility. There is a spread in the annihilation fields that does not depend upon the core polarity but is determined by energy minimization.

INVESTIGATION OF MAGNETIC DOMAIN CONFIGURATION  
AND VORTEX-ANTIVORTEX CREATION AND ANNIHILATION  
ON CoFeB PATTERNS

By

Jin Seock Ma

Thesis submitted to the Faculty of the Graduate School of the  
University of Maryland, College Park, in partial fulfillment  
of the requirements for the degree of  
Master of Science  
2011

Advisory Committee:  
Professor Romel Del Rosario Gomez , Chair  
Professor Chi H. Lee  
Professor Julius Goldhar

© Copyright by  
Jin Seock Ma  
2011

## Dedication

This thesis is dedicated to my lovely wife, Jeong A Park, my first baby, Hope, my mother, Myong Hee lee, my Father, Sung Rock Ma, my in-law parents, Soon Ok An, Young Ho Park my brother, Jang Hoon Ma, and, my brother's wife Hye Koung Kim.

## Acknowledgements

First of all, my greatest thanks and the glory for this thesis should be given to Jesus Christ.

The success of this research and thesis is possible due to the able and inspiring support of Dr. Romel Gomez, as my academic advisor. I really cannot imagine the current stage of this research without his strong advice and suggestions for completion of my research.

I would also like to thank the thesis committee members Professor Julius Goldhar, and Professor Chi H. Lee for being in my committee and providing valuable feedback on my work during discussions and thesis review.

I would express my gratitude to the Laboratory for Physical Science (LPS) for providing me a wonderful research environment. My special thanks are given to Dr. Charles Krafft, Dr. Michael Dreyer, Dr. Victor Yoon, and Dr. Dong Hoon Park for providing excellent technical support related to the fabrication tools. I also owe a debt of gratitude to my previous fellow group members, Dr. Jookyung Lee, Dr. Konrad Ascenbach, Dr. Seok Hwan Chung, Arman Arkilic and the current fellow group member Sowmya and Ting Xie for their friendly support and help.

The background for performing this research was prepared through coursework taken under the faculty in the Electrical Computer Engineering department and I highly appreciate their guidance in the same.

My precious gratitude is reached to my lovely wife Jeong A Park, my lovely baby, Hope, my parents Sung Rock Ma and Myong Hee Lee, my in-law parents, Young Ho

Park and Soon Ok An, my brother Jang Hoon Ma, my younger brother's wife Hye-Kyung Kim, and the members of Washington Nadulmok church, for their endless and friendly encouragement and support. Partial support from the University of Maryland MRSEC is also gratefully acknowledged.

Finally, I would like to thank Dr. Dave Bowen for proofreading and commenting on my manuscript.

# Table of Contents

<u>Dedication</u> .....	<u>ii</u>
<u>Acknowledge</u> .....	<u>iii</u>
<u>TABLE OF CONTENTS</u> .....	<u>v</u>
<u>LIST OF TABLES</u> .....	<u>viii</u>
<u>LIST OF FIGURES</u> .....	<u>ix</u>
<u>Chapter 1: Introduction</u> .....	<u>1</u>
<u>Chapter 2: Domain theory of ferromagnetism</u> .....	<u>3</u>
<u>2.1 General background</u> .....	<u>3</u>
<u>2.2 Domain theory</u> .....	<u>5</u>
<u>2.3. Magnetic energy</u> .....	<u>7</u>
<u>2.3.1 Magnetostatic or demagnetization energy</u> .....	<u>7</u>
<u>2.3.2 Anisotropy energy</u> .....	<u>8</u>
<u>2.3.2.1 Cubic anisotropy</u> .....	<u>8</u>
<u>2.3.2.2 Volume and surface &amp; interface anisotropy</u> .....	<u>9</u>
<u>2.3.2.3 Field induced anisotropy</u> .....	<u>10</u>
<u>2.3.3 Exchange energy</u> .....	<u>10</u>
<u>2.3.4 Zeeman energy</u> .....	<u>11</u>
<u>2.3.5 Formation of magnetic domain</u> .....	<u>12</u>
<u>2.4. Magnetic domain walls</u> .....	<u>13</u>
<u>2.4.1 Bloch wall</u> .....	<u>13</u>
<u>2.4.2 Néel wall</u> .....	<u>16</u>

<u>2.4.3 90° and 180° walls and cross-tie structure</u> .....	<u>18</u>
<u>2.4.4 Magnetic vortex</u> .....	<u>22</u>
<u>2.5 Property of CoFeB alloy</u> .....	<u>25</u>
<u>Chapter 3: Experimental procedure</u> .....	<u>26</u>
<u>3.1 Cleaning process</u> .....	<u>26</u>
<u>3.2 Formation of CoFeB patterns</u> .....	<u>26</u>
<u>3.3 Sputtering process</u> .....	<u>29</u>
<u>3.4 Lift-off</u> .....	<u>33</u>
<u>3.5 Annealing</u> .....	<u>34</u>
<u>3.6 Magnetic force microscopy (MFM)</u> .....	<u>35</u>
<u>3.6.1 Introduction</u> .....	<u>35</u>
<u>3.6.2 Principle of operation</u> .....	<u>35</u>
<u>3.7 Applying in-plane magnetic field with electromagnet</u> .....	<u>39</u>
<u>3.7.1 Electromagnet</u> .....	<u>39</u>
<u>3.7.2 Applying magnetic fields to the sample</u> .....	<u>43</u>
<u>Chapter 4: Results and Discussion</u> .....	<u>44</u>
<u>4.1 Magnetic domains into 7 categories</u> .....	<u>44</u>
<u>4.2 Interpretation of the MFM images with the aid of micromagnetic-modelling</u> ....	<u>47</u>
<u>4.3 Magnetic domain configuration with different thicknesses</u> .....	<u>50</u>
<u>4.4 Vortex-antivortex creation and annihilation in CoFeB patterns with a cross-tie wall</u> .....	<u>60</u>

<u>Chapter 5 : Future work</u> .....	<u>68</u>
<u>5.1 Control of core direction of vortex-antivortex with applying out-of plane magnetic field</u> .....	<u>68</u>
<u>5.2 Investigation of CoFeB patterns on MgO[100] substrate</u> .....	<u>69</u>
<u>5.3 FMR(Ferromagnetic resonanace) measurement of cross-tie walls on CoFeB patterns</u> .....	<u>72</u>
<u>Chapter 6 : Conclusion</u> .....	<u>77</u>
<u>Appendices</u> .....	<u>79</u>
<u>References</u> .....	<u>87</u>

## List of Tables

Table 2.1 Curie temperatures of some ferromagnetic materials .....	4
Table 3.1 Calibration data of applied voltages(+) and measured magnetization(+)	41
Table 3.2 Calibration data of applied voltages(-) and measured magnetization(-)	42
Table A.6 Fabrication procedure of CoFeB patterns on the Si substrate.....	84
Table A.7 Fabrication procedure of FMR device.....	85

## List of Figures

Figure 2.1 Hysteresis loop of ferromagnetic material.....	4
Figure 2.2 Schematic of the break-up of magnetization into domains.....	6
Figure 2.3 Schematic representation of a 180° domain wall.....	12
Figure 2.4 Schematic of a Bloch wall in a thin film.....	13
Figure 2.5 Replacement of the Bloch wall with a magnetized elliptic cylinder.....	14
Figure 2.6 Domain wall type of Bloch wall.....	15
Figure 2.7 Replacement of the Néel wall with a magnetized elliptic cylinder.....	16
Figure 2.8 Schematic of a Néel wall.....	17
Figure 2.9 Schematic of a 90° domain wall.....	18
Figure 2.10 Schematic of a 180° domain wall.....	19
Figure 2.11 Schematic of a cross-tie domain wall.....	20
Figure 2.12 Domain model of a cross-tie domain wall structure with a characteristic cross-tie spacing.....	22
Figure 2.13 Wall energy as a function of film thickness.....	26
Figure 2.14 Two types of magnetic vortex in a rectangular pattern and in disks.....	24
Figure 3.1 E-Beam writing design file for patterning of CoFeB islands.....	28
Figure 3.2 Images of after develop process and of after lift-off process.....	29
Figure 3.3 Image of sputtering process.....	31
Figure 3.4 DC Sputtering process.....	32
Figure 3.5 Lift-off process.....	33
Figure 3.6 Experiment process from sample preparation to MFM measurement.....	34
Figure 3.7 Principles of MFM Lift modes.....	36

Figure 3.8 Schematic diagram of MFM implementation.....	37
Figure 3.9 Schematic diagram of an electromagnet with a cooling system.....	40
Figure 3.10 Flow process of MFM measurement with electromagnet.....	43
Figure 4.1 Seven types of domain configurations.....	44
Figure 4.2 Magnetization pattern (Left) and MFM image(right) of a rectangular island with the size of 16 $\mu$ m x 8 $\mu$ m.....	49
Figure 4.3 MFM images of CoFeB islands with 7 nm thickness.....	50
Figure 4.4 MFM images of CoFeB islands with 13m thickness.....	51
Figure 4.5 MFM images of CoFeB islands with 19nm thickness.....	52
Figure 4.6 MFM images of CoFeB islands with 28nm thickness.....	53
Figure 4.7 MFM images of CoFeB islands with 37nm thickness.....	58
Figure 4.8 MFM images of CoFeB islands with 45nm thickness.....	54
Figure 4.9 MFM images of CoFeB islands with 52nm thickness.....	55
Figure 4.10 MFM images of CoFeB islands with 63nm thickness.....	56
Figure 4.11 MFM images of CoFeB islands with different thickness.....	57
Figure 4.12 Formation of vortices from saturated state.....	62
Figure 4.13 Annihilation of vortices from remanent to saturation.....	63
Figure 4.14 Plot of the location of all vortices and antivortices.....	65
Figure 5.1 Obtained MFM image and expected schematic illustrations of realized magnetization distribution.....	69
Figure 5.2 Fabrication process of CoFeB pattern using etching technique.....	70
Figure 5.3 Fabrication process of CoFeB pattern using lift-off technique.....	71
Figure 5.4 Fabrication process of FMR device.....	74

Figure 5.5 Microscopic images after formation of CoFeB ferromagnet and Ti/Au Contact pads.....	75
Figure 5.5 Microscopic images after formation of CoFeB ferromagnet and Ti/Au Contact pads.....	76
Figure A.1 MFM images of 16 $\mu$ m x 4 $\mu$ m CoFeB islands with applying magnetic fields .....	79
Figure A.2 MFM images of 16 $\mu$ m x 4 $\mu$ m CoFeB islands with applying magnetic fields .....	80
Figure A.3 MFM images of 9 $\mu$ m x 3 $\mu$ m CoFeB islands with applying magnetic fields .....	81
Figure A.4 MFM images of 9 $\mu$ m x 3 $\mu$ m CoFeB islands with applying magnetic fields .....	82
Figure A.5 MFM images of 9 $\mu$ m x 3 $\mu$ m CoFeB islands with applying magnetic fields .....	83
Figure A.8 Photolitho-mask designs of FMR device.....	86

## **Chapter 1. Introduction**

The experiments described in this thesis relate to the recently emerging and rapidly growing field of spin electronics, or “Spintronics”. Ferromagnetic materials like Ni, Co, or Fe have the magnetic property of a collective interaction between the electron spins. This characteristic can be explained as a magnetic moment, which leads much interest concerning basic physics and technical applications[1][2].

In this thesis, the investigation is focused on magnetic domain configurations with different CoFeB thicknesses and the dynamics of vortices and their topological counterparts, the anti-vortices. A novel theoretical description of the core trajectory in the linear and nonlinear regime of excitation is outlined. The switching process of the orientation of the core magnetization is described, and possible applications of vortex random access memory (VRAM) or of an anti-vortex as anti-vortex random access memory (AVRAM) are presented[3].

The main purpose of this thesis is to study the creation and annihilation of the vortex and anti-vortex pairs in cross-tie walls on CoFeB islands in the presence of externally applied magnetic fields.

This thesis is organized as follows.

Chapter 2 reviews the relevant fundamental background material in ferromagnetism. The phenomenon of the domain formation in the ferromagnetic islands will be explained along with a brief account of the relevant theories on magnetic energies, magnetic domain walls, and magnetic vortex-antivortex pairs.

Chapter 3 provides the discussion on the fabrication process of CoFeB island devices using e-beam writing and CoFeB thin film deposition using direct current sputtering in an ultrahigh vacuum (UHV) system. This chapter also describes the basics of magnetic force microscopy (MFM), the workhorse experimental technique used throughout this work. MFM measurement was performed with externally applied magnetic field by the use of an electromagnet[5].

In chapter 4, the results of this experiment are presented and discussed. MFM images of the remanent state in CoFeB islands of different thicknesses placed on Si substrate are shown along with micro-magnetic modeling of the CoFeB island. Next the vortex-antivortex creation and annihilation in CoFeB patterns are discussed.

Chapter 5 deals with the future work related to this investigation. First, the possibility of controlling the core direction of vortex-antivortex pairs in CoFeB islands with externally applied out-of plane magnetic fields is explained[6]. Fabrication processes are described for creating CoFeB patterns on an MgO substrate, instead of a Si substrate. Similarly, a ferromagnetic resonance (FMR) measurement experiment using the vortex-antivortex pairs of CoFeB patterns is introduced the expected behavior of the device is briefly described[7][8].

In chapter 6, some conclusions of this thesis are summarized.

In the appendix, Magnetic Force Microscopy (MFM) images with applied magnetic fields in the CoFeB island of  $9\mu\text{m} \times 3\mu\text{m}$  are shown, as well as the details concerning the device structure and fabrication process of the device are included in the appendix. This appendix is geared to those who wish to replicate the experiment and recipes.

## Chapter 2. Domain theory of Ferromagnetism

### 2.1 General Background

Ferromagnetic materials like iron, nickel, or cobalt exhibit a long-range ordering phenomenon at the atomic level which causes the unpaired electron spins to line up parallel with each other in a region called a magnetic domain[9][10][11]. Ferromagnetism exhibits itself in the fact that a small externally imposed magnetic field, say from a solenoid, can cause the magnetic domains to line up with each other and the material is said to be magnetized. The driving magnetic field will be increased within the material by a large factor, which is the relative permeability for the material. Another attribute of ferromagnetism is that the magnetization can non-linear with respect to the applied magnetic field. This property is called a hysteresis. A generic hysteresis curve is shown Fig. 2.1, where the y-axis is the magnetic induction,  $\vec{B} = \mu_o(\vec{H} + \vec{M})$ ,  $\vec{H}$  is the applied magnetic field and  $\vec{M}$  is the magnetization. The fraction of the saturation magnetization that is retained when the driving field is removed is called the remanence of the material, which for obvious reasons is a significant factor in permanent magnets. The field that causes the zero-crossing of the magnetic induction is referred as the coercivity of the material. This parameter is of paramount importance in magnetic recording, memory and field sensing applications.

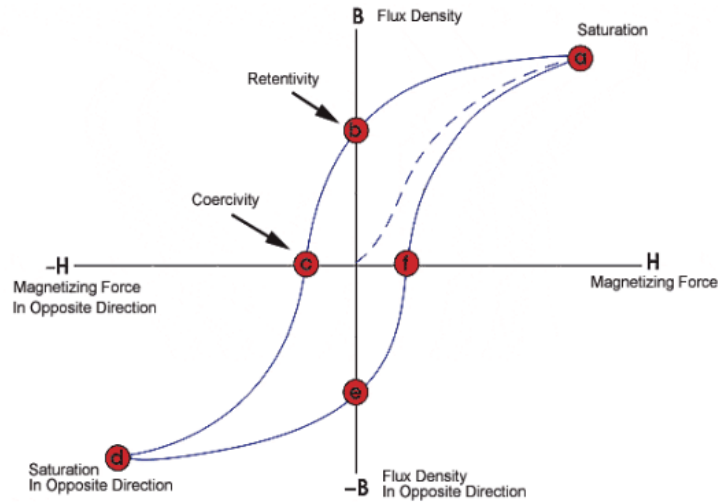


Figure 2.1 Hysteresis loop of ferromagnetic material.

All ferromagnets have a maximum temperature where the ferromagnetic property is lost as a result of thermal agitation. This temperature is defined as the Curie temperature and a short list for some ferromagnetic materials are shown in the table below[12].

Material	Curie Temperature(°C)
Fe	770
Co	1115
Ni	354
CoFe	1327
MnAs	45
EuO	-4
Fe <sub>2</sub> B	742

Table 2.1 Curie temperatures of some ferromagnetic materials.

## 2.2 Domain Theory

The premise of domain theory of ferromagnetism is the fact that a ferromagnetic material exhibits spontaneous magnetization in the demagnetized state. Within a domain, large numbers of atomic moments are aligned, typically  $10^{12} \sim 10^{18}$ , over a large volume [11]. In any given domain, the magnetization is saturated and always lies in the so-called crystallographic easy axis in the absence of an externally applied field.

Domains result because of the lowering of the total energy of the system, which, in general, arise from the competition between the lowering of magnetostatic energy against the cost of domain wall formation. This process is illustrated schematically in Figure 2.2, starting a uniformly magnetized specimen in Fig. 2.2 a). The magnetic poles (or surface magnetic charges,  $\vec{M} \cdot \hat{n}$ ,  $\hat{n}$  being the surface normal unit vector) at the surface of the specimen produce an internal field that is opposite to the direction of magnetization. This is called the demagnetizing field,  $H_d$ . The exact analytical expression for the demagnetizing field can be calculated only in the case of an ellipsoid, but in general, demagnetizing field is inversely proportional to the aspect ratio (length to diameter). In fact, it can be shown that the magnetostatic energy goes as  $1/N$ .

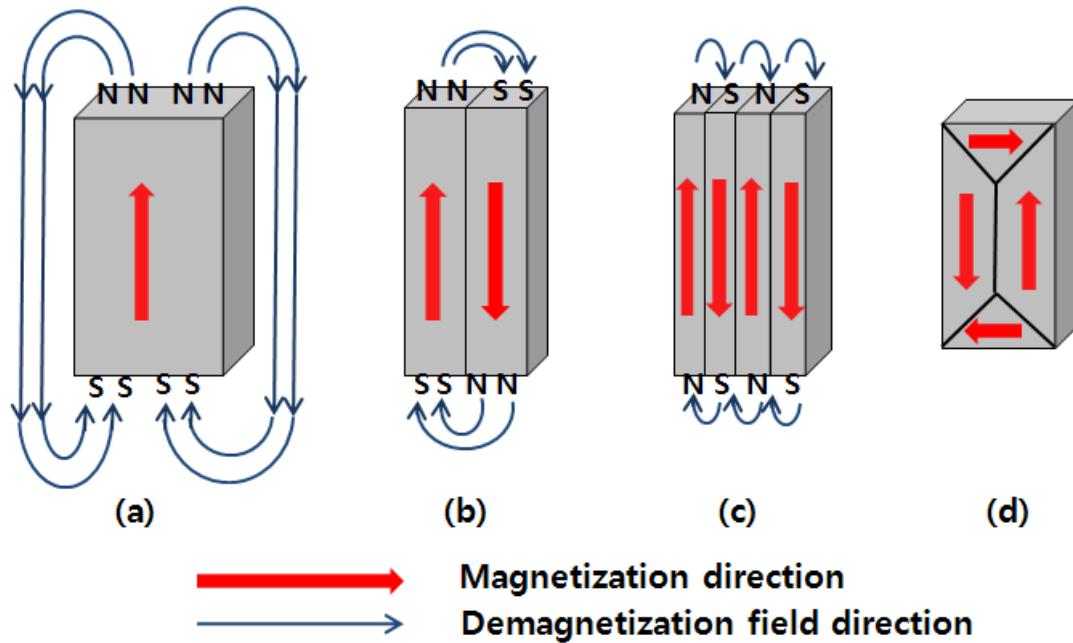


Figure 2.2 Schematic of the break-up of magnetization into domains.

Another mechanism to lower the energy, depicted in figure 2.2(d) is the formation of so called “*closure domain*” patterns. The magnetization is always parallel with the surface, thus producing no surface charges, no demagnetization field and zero magnetostatic energy. The magnetostatic energy is contributed by the variation of the magnetization along the domain boundaries corresponding to the volume charge density  $(-\nabla \cdot \vec{M})$ . Closure patterns are found on materials that do not have a strong uniaxial anisotropy that force adjacent domains to be at  $180^\circ$  to each other.

## 2.3 Magnetic energies

In the films used in this study, the relevant magnetic energies are magnetostatic, exchange, anisotropy and Zeeman energy.

### 2.3.1 Magnetostatic or Demagnetization energy

Magnetostatic energy originates from the classical interactions between magnetic dipoles and is explained by the effect of magnetization  $\vec{M}$ , the magnetic-dipole moment per volume, which arises from the alignment of atomic magnetic dipoles. In magnetic materials, electron spins lead to the creation of magnetic dipoles. Even though the dipole strength is not affected greatly by the orbital motion of electrons, it has an important effect on the formation of magnetic anisotropy[10].

In a single magnetic domain with a finite size, there exists a great magnetostatic energy, which leads to the separation of the volume magnetization into localized domains. Multiple domains will be created in a material until an energy equilibrium is reached between magnetostatic energy and domain wall energy.

In addition, the magnetostatic energy can be easily explained with the example of an infinite plane magnetic film magnetized uniformly perpendicular to the surface.

The stray field,  $\vec{H}_{stray}$ , is generated by magnetic dipoles in the film,  $\vec{M}$ . Surface charges create a field inside the film which has the same amplitude as  $\vec{H}_{stray}$ , but directs opposite to  $\vec{M}$ , called demagnetizing field,  $\vec{H}_d$ .

In this case where the magnetostatic energy has the same magnitude as the demagnetizing energy, the energy is given with  $\overset{\cup}{M}$  and  $\overset{\cup}{H}_d$  as

$$K_d = -\mu_0 \int_V \vec{M} \cdot \vec{H}_d dV = -\mu_0 \int_V \vec{M} \cdot \frac{\vec{H}}{2} dV = \frac{\mu_0}{2} M_S^2, \quad (2.1)$$

In equation 2.1,  $\overset{\cup}{M}$  is taken as the saturation magnetization,  $M_S$ , and  $\overset{\cup}{H}$  is the total field sum of  $\overset{\cup}{H}_{stray}$  and  $\overset{\cup}{H}_d$ .

$$\overset{\cup}{H}_{stray} = \overset{\cup}{H}_d \rightarrow \overset{\cup}{H}_T = \overset{\cup}{H}_{stray} + \overset{\cup}{H}_d = 2 \overset{\cup}{H}_d \quad (2.2)$$

### 2.3.2. Anisotropy energy

The direction of magnetization related to the well-defined crystallographic axes of the material also affects the magnetic energy, which is defined as the magnetic anisotropy energy. The magnetic anisotropy energy is usually generated from spin-orbit interaction of the electrons. In the case of ferromagnetic materials, there exists a uniaxial anisotropy regardless of crystallization state or composition. Usually the anisotropy is determined along the crystal orientation in pure crystal materials.

Anisotropy is created from the following sources: separation of the crystal structure at the substrate interface, anisotropic modulation of atoms, or by alignment of interface/surface defects.

#### 2.3.2.1 Cubic anisotropy

The cubic anisotropy energy is usually explained as magnetocrystalline in nature, so it results from the interaction of the atomic magnetic moments with the intrinsic symmetry of their crystal structure via a spin-orbit interaction.

The cubic anisotropy energy density is calculated by

$$E_c = K_1(m_x^2 m_y^2 + m_x^2 m_z^2 + m_y^2 m_z^2) + K_2 m_x^2 m_y^2 m_z^2 + \dots, \quad (2.3)$$

In, equation 2.3,  $K_1$ ,  $K_2$ , *etc.* are the anisotropy constants, and  $m_x$ ,  $m_y$ , and  $m_z$  are the magnetization of  $x$ ,  $y$  and  $z$  crystal axes.  $K_i$  is the  $i_{th}$  order anisotropy constant.

### 2.3.2.2 Volume, surface and interface anisotropy

In the case of magnetic films with nano-sized thickness, surface and interface anisotropy should be considered due to missing adjacent atoms. A much stronger anisotropy was observed for single atomic transition metal films, in comparison to bulk materials. In magnetic films with uniaxial anisotropy perpendicular to the film plane, the anisotropy energy is symmetric. So the surface anisotropy energy density is expressed by

$$E_S = K_S \sin^2 \theta \quad (2.4)$$

In equation 2.4,  $K_S$  is the surface energy and  $\theta$  is the angle between the magnetization and the film normal. The volume anisotropy is insignificant for magnetic films with nano-sized thickness. In hexagonal or tetragonal crystals, a uniaxial volume anisotropy ( $K_U$ ) normal to the film exists for a certain thickness range, where the volume anisotropy energy density is calculated by

$$E_V = K_{U1} \sin^2 \theta + K_{U2} \sin^4 \theta \quad (2.5)$$

In equation 2.5,  $\theta$  is the angle between the magnetization and the anisotropy axis and the odd power is not considered because of time inversion symmetry.

The total anisotropy energy density is written as

$$E = E_V + \frac{E_s}{d} \quad (2.6)$$

### 2.3.2.3 Field induced anisotropy

Uniaxial anisotropy is observed in ferromagnetic materials with an applied magnetic field and applied heat. As a result, the direction of magnetization is affected by the direction of applied magnetic field, so it is defined as a field-induced anisotropy. Sometimes this induced anisotropy is found in single crystal films. In addition, this type of induced anisotropy can be explained by the magnetic annealing effect. The film is usually strained in the direction of the field, when it is deposited at some temperature with an applied magnetic field. As the temperature decreases to the room temperature, the film adheres to the substrate. Subsequently, the atoms cannot diffuse to relieve the strain caused by the magneto restriction and the magnetic anisotropy along the direction arises from the anisotropy distortion.

### 2.3.3 Exchange energy

Exchange energy is described by the basic interaction which leads to cooperative magnetic ordering. Between  $S_i$  and  $S_j$ , *with* scales with the exchange integral,  $J$ (dimension ; J), the exchange energy is expressed by

$$E_{ex} = -J_{ij} \vec{S}_i \cdot \vec{S}_j \quad (2.7)$$

In the equation 2.7,  $S_i$  and  $S_j$  are the unit vectors of interacting spins on two atoms.

The exchange interaction is explained by the Coulomb interaction between the Pauli principle and electron charges. In a magnetic domain wall, the exchange energy is also explained by a continuous model of spin rotation in a one-dimensional domain wall.

So the sum of  $E_{ex}$  inside the wall is expressed as

$$E_{ex} = A \left( \frac{d\theta}{dx} \right)^2 \quad (2.8)$$

In the equation 2.8,  $A = s^2 a_L^2 J N \nu / 2$  is the temperature dependent exchange stiffness constant (J/m),  $s$  is the spin quantum number ( $S=1/2$ ), and  $a_L$  is the lattice constant.  $N \nu$  indicates the number of nearest-neighbor atoms per unit volume.  $\theta$  is the angle with respect to the easy axis of magnetization. In the case of simple cubic (SC) and body centered cubic (BCC),  $J$  will be

$$J = 0.54 K_b T_c \quad (2.9)$$

In the equation 2.9  $K_b$  and  $T_c$  are the Boltzmann constant and the Curie temperature, respectively. The exchange energy favours a magnetic domain wall as wide as possible.

#### 2.3.4. Zeeman energy

Zeeman energy is the term which arises from the interaction energy of the magnetization vector field  $\vec{M}$  with an external magnetic field  $\vec{H}_{ext}$ .

$$E_Z = \mu_0 \int \vec{M} \cdot \vec{H}_{Ext} dV \quad (2.10)$$

### 2.3.5 Formation of magnetic domains

In general, the minimization of the total magnetic energy which is the sum of magnetostatic, exchange, anisotropy and Zeeman energy, determines the magnetic domain sizes.

$$\square = E_{ex} + E_A + E_Z + E_d \quad (2.11)$$

The occurrence of a domain increases the whole energy of the specimen, so that division into domains persists only as long as the reduction in magnetostatic energy is greater than the energy required to form the domain wall. The energy of a domain wall depends on the wall area and the domain width, which in turn are determined by the intrinsic characteristics of a material such as the magneto-crystalline anisotropy and the strength of the exchange interaction between neighboring atoms. Strong magneto-crystalline anisotropy will favor a narrow wall, whereas a strong exchange interaction will favor a wider wall. A bulk minimum energy determines the specific size and number of domains. The effect of the Zeeman energy is to favor the growth of domains whose magnetization is parallel to the applied field.

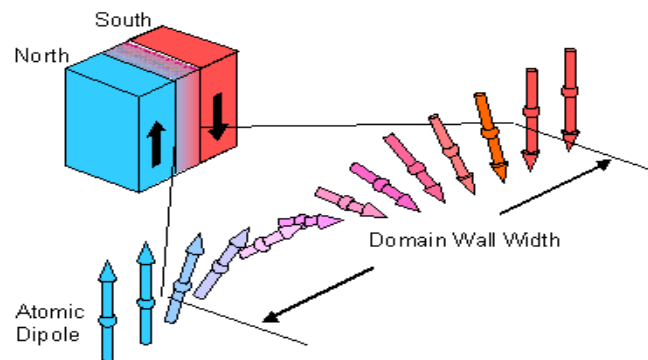


Figure 2.3 Schematic representation of a 180° domain wall.

### 2.4 Magnetic domain walls

## 2.4.1 Bloch wall

In ferromagnetic material like Fe, Co or Ni, the magnetic structure of films usually consists of magnetic domains, inside of which the magnetization is largely uniform, separated by transitional regions where the magnetization vector rotates. These transition regions are defined as magnetic domain walls. Both static and dynamic magnetic properties of multi-domain thin films depend crucially on the structure of the domain walls. In addition, magnetic domains will be formed in order to reduce the material energy, while between the domains a domain wall will also be created to transition different directions of magnetization. Usually there are two types of magnetic domains walls: Bloch walls and Neel walls. Bloch walls are usually energetically more favorable in bulk materials.

In figure 2.4, a cross section of a thin film with a domain wall between two anti-parallel in-plane domains is described [13]. The direction of the magnetization in the domain wall is perpendicular to the plane of the film and the magnetic moments in the wall rotate about an axis perpendicular to the wall axis.

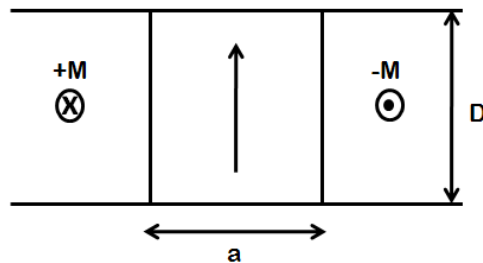


Figure 2.4 Schematic of a Bloch wall in a thin film.

The thickness  $D$  of the film is comparable to the width of the wall,  $a$ . Since magnetic poles are created on the film surface along the wall axis, a demagnetizing

field will exist in the wall. The energy related to the demagnetizing field can be estimated by Néel's approximation. In Néel's approximation, the demagnetizing energy of the wall is equivalent to the demagnetizing energy of an elliptic cylinder with a magnetization along its easy axis and included in the space of the magnetic domain walls shown in figure 2.5.

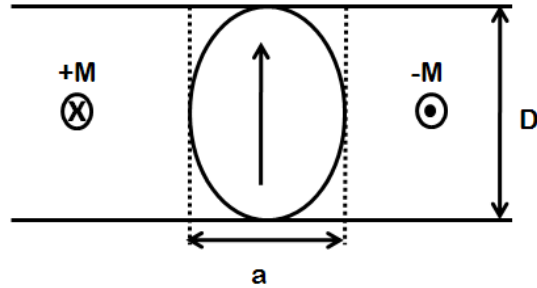


Figure 2.5 Replacement of the Bloch wall with a magnetized elliptic cylinder.

The demagnetizing surface energy can be calculated by the following

$$\mathcal{E}_m = \frac{2\pi a^2 M^2}{a+D} \quad (2.12)$$

In equation 2.12,  $a$  is the width of the wall and  $D$  is thickness of the wall. For calculating the total energy of the Bloch wall, the surface energy of the wall,  $\sigma_0$  will be added to the total wall energy from anisotropy and exchange interaction with the following equation[14] :

$$\mathcal{E}_w = \frac{1}{2} \sigma_0 \left( \frac{a_0}{a} + \frac{a}{a_0} \right) \quad (2.13)$$

The total Bloch wall energy can be calculated with the sum of the demagnetizing energy, and the wall energy of anisotropy and exchange interaction[14].

$$\mathcal{E}_B = \frac{1}{2} \sigma_0 \left( \frac{a_0}{a} + \frac{a}{a_0} \right) + \frac{2\pi a^2 M^2}{a+D} \quad (2.14)$$

The Bloch domain wall type is shown in the figure 2.6.

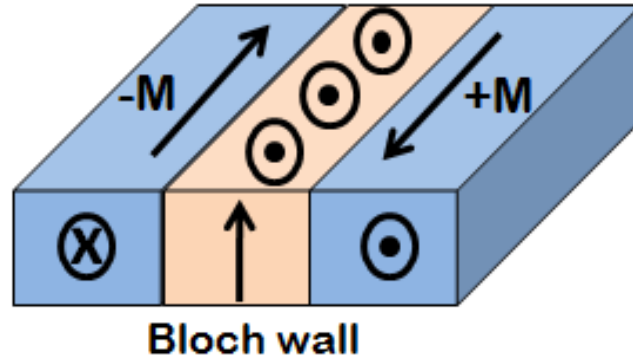


Figure 2.6 Domain wall type of Bloch wall.

#### 2.4.2 Néel wall.

Néel walls will replace the Bloch wall when the film thickness becomes smaller than the wall width, because of the large increase in the wall energy. In a Néel wall, spins rotate in the film plane and the widths of Néel walls are difficult to define. The Néel wall can be analyzed with a magnetized elliptic cylinder model and figure 2.7 shows a cross-section depiction of a Néel wall in a film and its approximation.

In a Néel wall, the wall energy of anisotropy and exchange interaction will also be added to the demagnetizing energy and the total energy of Néel wall is the same as that of a Bloch wall[9][11].

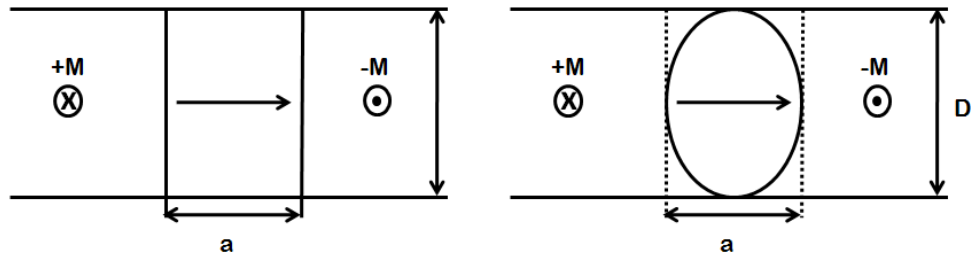


Figure 2.7 Replacement of the Néel wall with a magnetized elliptic cylinder.

To first order, the magnetostatic energy of the Néel wall can be assumed to be the same as the demagnetizing energy of the elliptic cylinder shown in figure 2.8. The demagnetization surface energy of the wall is then just[14]

$$\mathcal{E}_m = \frac{2\pi a^2 DM^2}{a+D} \quad (2.15)$$

The anisotropy and exchange energy is unchanged from the form given in equation 2.15 so that total energy of the Néel wall can be written

$$\mathcal{E}_N = \frac{1}{2} \sigma_0 \left( \frac{a_0}{a} + \frac{a}{a_0} \right) + \frac{2\pi a DM^2}{a+D} \quad (2.16)$$

The Néel wall is shown in the figure 2.8.

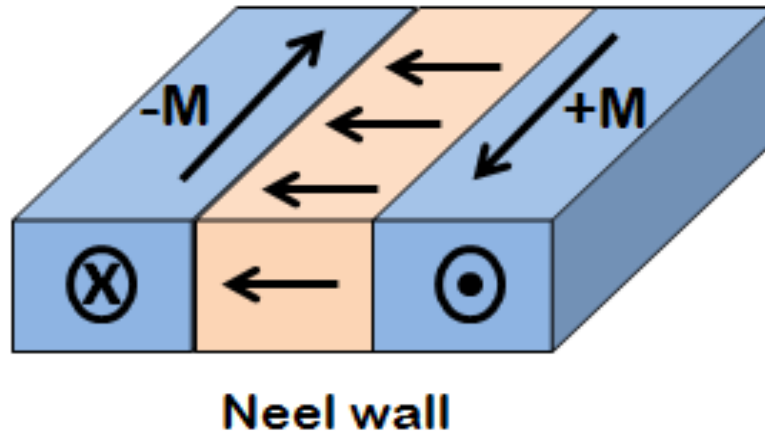


Figure 2.8 Schematic of a Néel wall.

### 2.4.3 90° and 180° walls and cross-tie structure

There are two orientations of domain wall, 90° walls and 180° walls, which are created according to the degree of formed wall in Bloch and Néel walls. A 90° wall

divides two domains with magnetizations perpendicular to each other. As shown in figure 2.9, a  $45^\circ$  angle center-point magnetization between the two domains is formed in the  $90^\circ$  wall[9].

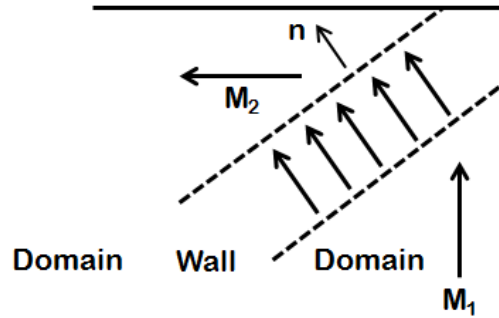


Figure 2.9 Schematic of a  $90^\circ$  domain wall.

In the case of a  $180^\circ$  wall, adjacent domains have an anti-parallel direction of magnetizations. As shown in figure 2.10, the  $180^\circ$  wall has the role of separating the domains and the wall center-point magnetization is perpendicular to each domain[9].

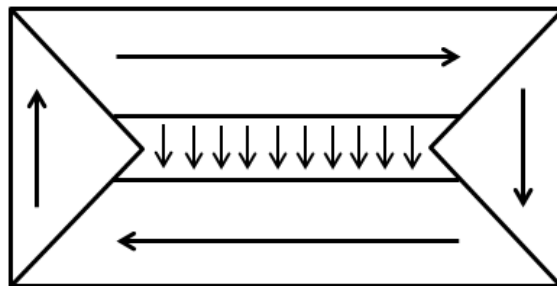


Figure 2.10 Schematic of a  $180^\circ$  domain wall.

The cross-tie wall is observed in somewhat thicker films. It is like a periodic microstructure of Néel walls and Bloch walls. Instead of a single Néel wall, the material chooses an energetically favorable structure of longer, but lower-angle Néel walls. In the case of a long  $180^\circ$  wall, the exchange energy can become very high.

Lower exchange energy is found in wall structures called cross-tie walls, which will be created in the  $180^\circ$  walls. While as every spin makes flips in a  $180^\circ$  wall, groups of spins will become aligned according to the same direction and the direction usually will be changed with  $180$  angle. In addition, a vortex-antivortex structure will be created at the points in which the direction of magnetization of a  $180^\circ$  wall will reverse due to the formation of closure loop of spins.

As the magnetostatic energy is continuously reduced, the closure loops contribute to the formation of vortex and anti-vortex structures.

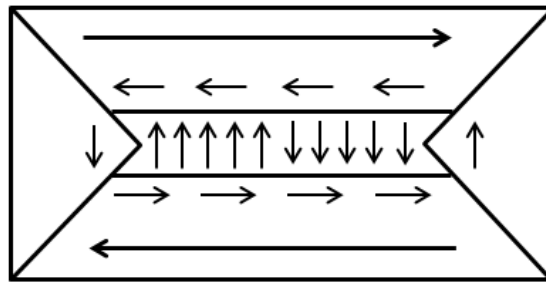


Figure 2.11 Schematic of a cross-tie domain wall.

Cross-tie walls are characterized by an alteration of Bloch-like vortex and anti-vortex transitions along the domain wall segmented by  $90^\circ$  Néel walls of opposite chirality in figure 2.11[15]. As the specific energy of a  $90^\circ$  Néel wall is significantly lower than that of a  $180^\circ$  Néel wall, the complicated  $90^\circ$  domain wall network of the

cross-tie wall saves energy, compared with a regular 180° domain wall. In the cross-tie arrangement the magnetic flux of the long-range magnetic tails is partially closed in the vicinity of the walls. The occurrence of cross-tie walls in low anisotropy CoFeB films is limited to a narrow thickness of ferromagnetic material ( $t_F$ ) range. Below  $t_F \approx 10$  nm, 180° Néel walls exist and above  $t_F \approx 100$  nm, asymmetric Bloch walls form. In the intermediate of ferromagnetic material thickness of cross-tie wall stability, the cross-tie spacing  $\lambda_{ct}$  scales inversely with the magnetic anisotropy energy constant  $K_{u,eff}$  or anisotropy field  $H_{k,F}$ [16]. This behavior is found experimentally and only basic features can be modeled theoretically[17][18]. For a given film thickness, the experimentally found dependency of  $\lambda_{ct}$  on anisotropy of a single F layer is

$$\lambda_{ct} \propto (K_{u,eff})^{-n} = (H_{k,F})^{-n}, \quad (n = 0.5, \dots, 1.0) \quad (2.17)$$

In equation 2.17, the exponent  $n$  depends on the ferromagnetic film thickness. This relation provides merely a rough guidance for the change of  $\lambda_{ct}$  with anisotropy and is only valid for small values of anisotropy. Nevertheless,  $\lambda_{ct}$  serves as a sensitive measure of changes in the effective anisotropy in ferromagnetic thin films. Above a certain value of anisotropy, the cross-tie wall transforms into a symmetric 180° Néel wall. This is due to an increased energy contribution from the Bloch lines inside the domain wall with smaller cross-tie spacing, increased Bloch line density.

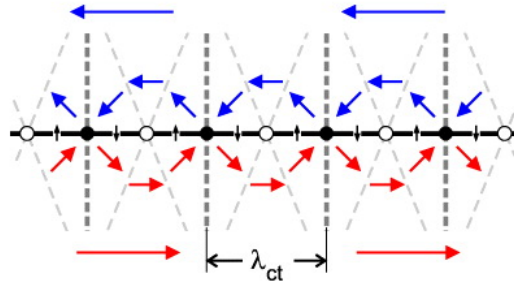


Figure 2.12 Domain model of a cross-tie domain wall structure with a characteristic cross-tie spacing  $\lambda_{ct}$ [19].

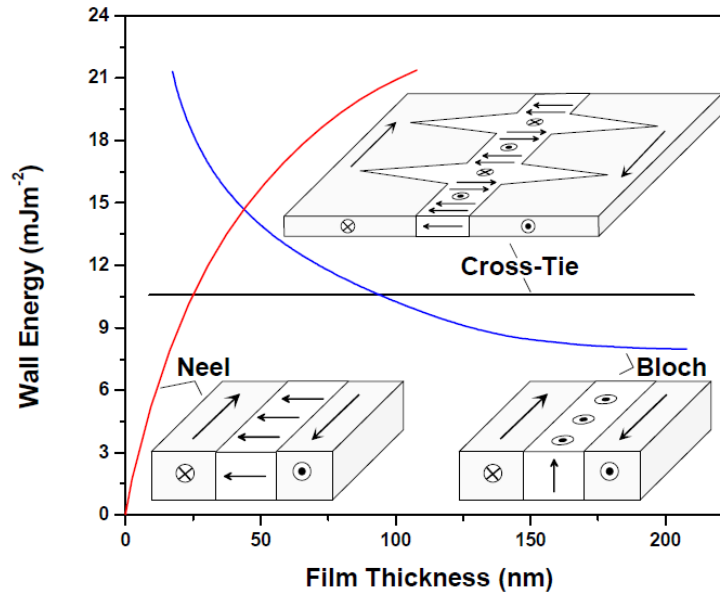


Figure 2.13 Wall energy as a function of film thickness[14].

What is of particular interest is a comparison between Bloch, Neel and Cross-Tie walls as a function of the film thickness. In figure 2.13, the transition point above Néel type walls are more preferable and below which Bloch walls preferred[14].

## 2.4.4 Magnetic vortex

As explained in the previous chapter, the Bloch wall is replaced by Néel walls in thin ferromagnetic material. Magnetic vortices are created when two Néel walls cross with each other or when the circular dot domain thickness in the ferromagnetic material is much smaller than the circular diameter of the dot[20][21][22]. Magnetic vortices are magnetic configurations with an in-plane magnetization but an out-of-plane center region of the magnetization. They are formed in soft magnetic thin-film elements with a lateral size of a few hundred nanometers to a few microns when the demagnetization energy forces the magnetization to align parallel to the sample's surface, which for thin films is the in-plane direction[23]. At the vortex's center region, where magnetization vectors would align antiparallel to each other, the exchange energy leads to an alignment of the magnetization vectors out-of-plane either up or down and thus forms the magnetization core. Magnetic vortices possess a rotationally symmetrical in-plane magnetization with the vortex core as the symmetry axis[24].

The counterpart of a magnetic vortex is a magnetic structure with similar properties, known as an antivortex. Both vortex and antivortex have a magnetic core which is magnetized perpendicular to the plane. A vortex and an antivortex can annihilate when they meet. Besides the fact that the annihilation is connected with an emission of spin waves, not much is known about the magnetization dynamics of the vortex-antivortex annihilation process.

The annihilation of a vortex and an antivortex has been investigated with finite-element micro-magnetic simulations based on the Landau-Lifshitz-Gilbert equation.

A specific description of this previously unexplored fundamental magnetization process was produced by those calculations. As a result, it is shown that the process is affected strongly by the relative direction of the core magnetization of both the vortex and the antivortex[25][26][27][28][29].

If the core direction of the vortex and antivortex are antiparallel to each other, the annihilation process includes the propagation of a Bloch point, which leads to a burst like dissipation of exchange energy via spin waves. Considering the proposed use of magnetic vortices in data storage and magnetologic approaches, it will be necessary to manipulate the dynamic property well. Analyzing the annihilation dynamics of a vortex and an antivortex is a significant task in order to reach a precise description of the complicated dynamic magnetization processes containing the temporary formation of vortices[30].

Creation and annihilation of magnetic vortices and antivortices can only be possible *pairwise* and never individually. The perpendicular orientation of the magnetization in the vortex and antivortex cores is induced due to the ferromagnetic exchange interaction. A full in-plane magnetization would lead to a singularity of the exchange energy density, which is avoided if the magnetization turns out of the plane. The orientation of the magnetization in the core is often defined as the *polarization*. Unlike the vortex structure, an isolated antivortex is not stable because it does not develop naturally. An antivortex can be created in cross-tie domain wall structures, where they are enclosed by two vortices with the same sense of rotation[31][32].

Figure 2.14 shows two types of magnetic vortex-antivortex pairs in a rectangular pattern and in disks of a CoFeB thin film.

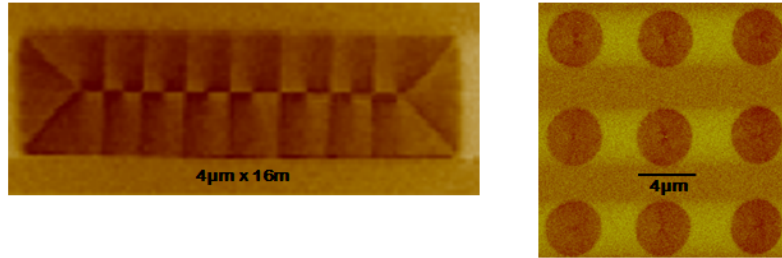


Figure 2.14 Two types of magnetic vortices in a rectangular pattern(left) and in disks(right).

## 2.5 Properties of CoFeB alloy

In recent years, CoFeB alloy has recently attracted much attention for magnetic applications like high tunneling magnetoresistance (TMR)-magnetic tunnel junction(MTJ) devices. In the case of single layer CoFeB film, it has a high saturation magnetization, a near zero hard axis coercivity, a low easy axis coercivity , extremely high permeability, and high anisotropic magnetoresistance. In the structure of an MTJ device, CoFeB electrodes might be crystallized locally near the interfaces because the MgO[001] layer could act as a template to a crystallize CoFeB layer. Basically, CoFeB shows similar properties to CoFe and has replaced CoFe for a higher TMR effect[33][34].

The conduction band of CoFeB has 4s and 3d subbands. A significant property of this band structure is that the effective mass of a 3d electron is much greater than one of 4s electrons:  $m_{4s} \sim 1/10 m_{3d} \sim m_e$ , where the  $m_e$  is free electron mass. As a result, the

4s electrons behave almost as free electrons and are extremely mobile charge carriers. By contrast, the 3d electrons are much slower due to their heavy mass, and they can be considered mostly as localized around a single atom. Because of the intra-atomic exchange, each electron with spin  $\pm 1/2$  acquires additional energy and one band splits into two corresponding to the two spin values.

## **Chapter 3. Experimental procedure**

### **3.1 Cleaning process**

Before device fabrication, a Si/SiO<sub>2</sub> wafer is cut into 10 mm x 10 mm pieces and cleaned in order to remove residual organic material and particles. First, a device is put in Chloroform liquid T = 100 °C for 20 minutes to get rid of residual organic material, then cleaned for five minutes in an ultrasonic cleaner. The device is cleaned again in an ultrasonic cleaner by Acetone and Methanol for ten minutes and five minutes, respectively. It is rinsed with DI-water and dried by N<sub>2</sub>-gas. In order to remove remaining moisture, it is baked on a 90 °C hot plate for 1 minute.

### **3.2 Formation of CoFeB patterns**

CoFeB islands are patterned by e-beam lithography. First, PMMA 495A(4%) is coated on the cleaned device and baked for fifteen minutes at 170 °C, and again PMMA 950K(2%) is coated on the device and baked for 15 minutes at a temperature of 170 °C. For e-beam lithography, a double-layer structure is formed by PMMA 495A and PMMA 950K, positive Electron-beam Resist(ER)s and the acceleration voltage and area dose are respectively 50 KV and 250  $\mu\text{C}/\text{cm}^2$ . The sensitivity of PMMA is controlled by the molecular weight of PMMA. Post-baking is performed after spinning of each PMMA layer. The top layer acts to mask the bottom layer, which is more sensitive to exposure and development, giving the sharp under-cut of the bottom layer which makes the lift-off process easier. The bottom layer should be at least two times thicker than the film thickness to prevent the film from touching the

bottom PMMA layer. However, thicker PMMA makes pattern resolution worse. In order to pattern on the micro or nano-meter scale, the focusing level of an electron beam is very important and the size of an electron beam is optimized at 30 nm ~ 40 nm.

The size of the CoFeB patterns varies from 250 nm x 250 nm to 16 $\mu$ m x 16 $\mu$ m and the thickness of the CoFeB patterns also varies from 6nm, 13nm, 18 nm, 28nm, 35nm, 48nm, 50nm, to 63nm . The edge-to-edge distance between the CoFeB patterns is 10  $\mu$ m. IPA:MIBK(1:3) is used as a developer material and is developed for nearly 60 seconds. Figure 3.1 shows the images of the CAD design showing the outlines of various patterns of the sample. Before CoFeB deposition, O<sub>2</sub> plasma ashing is performed in order to remove the residue of the e-beam resist. At 100W of RF power and a base pressure of 200 mTorr, O<sub>2</sub> plasma is applied to the e-beam patterned sample for fifteen seconds.

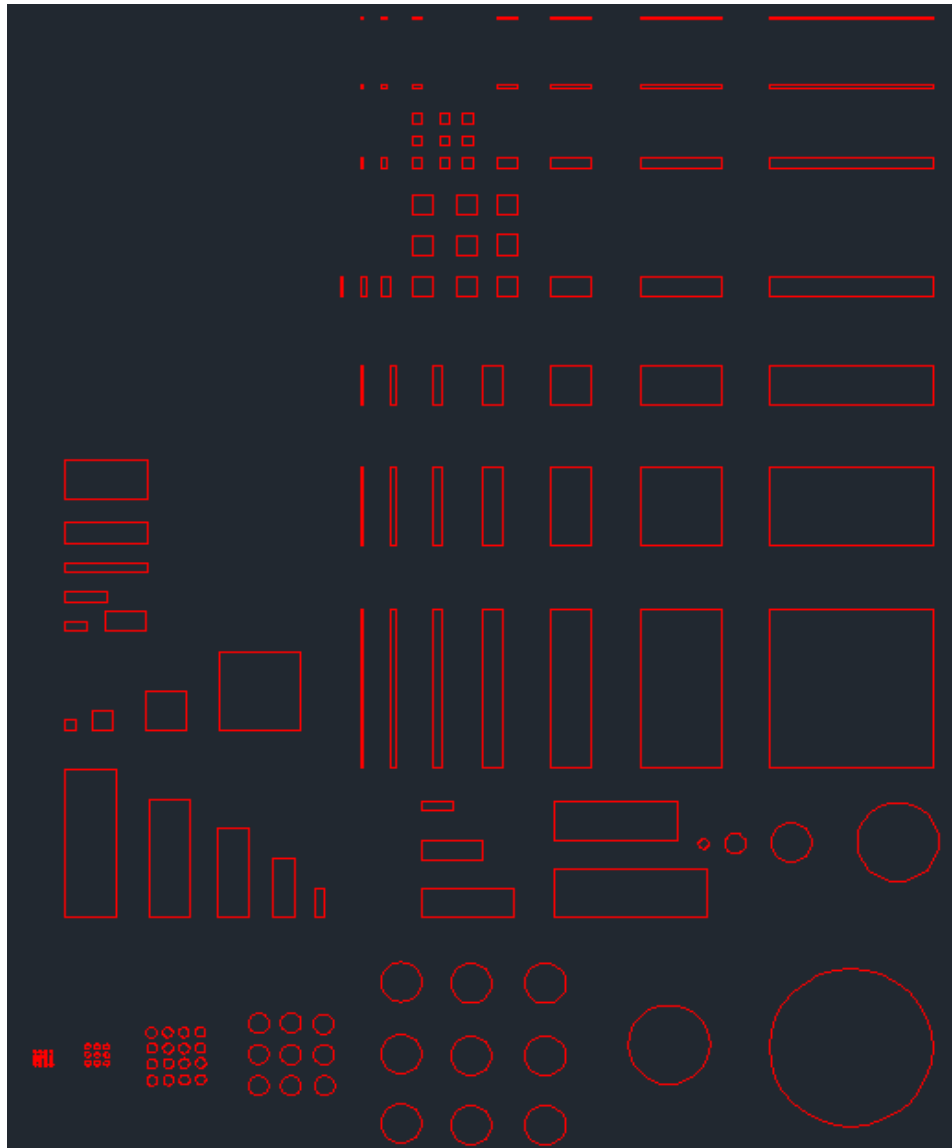


Figure 3.1 E-Beam writing design file for patterning of CoFeB islands.

For the formation of the domain structure, CoFeB is deposited with a DC magnetron sputter from a Co<sub>60</sub>Fe<sub>20</sub>B<sub>20</sub> target under a base pressure of  $1 \times 10^{-6}$  Torr for ten minutes. After the lift-off process, the devices were annealed at a constant temperature of 400 °C for 1hour.

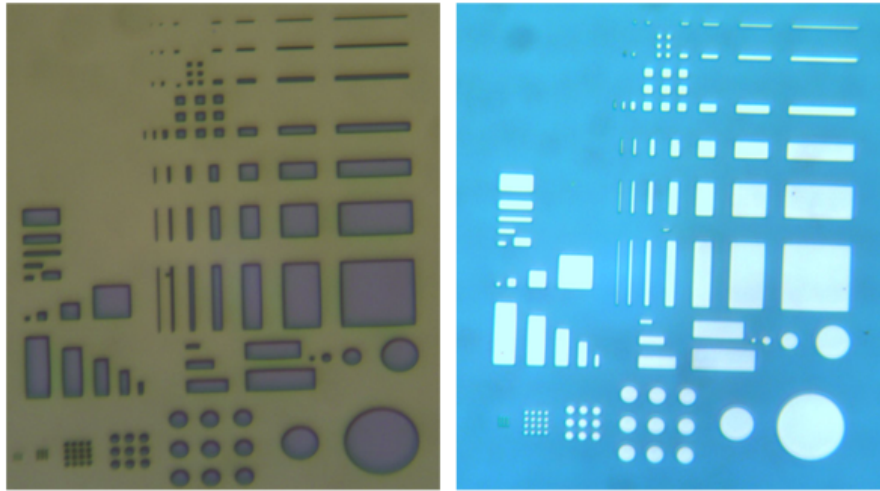


Figure 3.2 Images after develop process(left) and after lift-off process (right).

### 3.3 Sputtering process

The sputtering process is widely used in the semiconductor industry, mainly for the creation of metal films or the modification of electrical characteristics. In the optics industry, dielectric material film is necessary. Plasma sputtering is also an important branch in physical vapor deposition (PVD) technology. In 1852, the sputtering deposition was initially found by William Robert Grove and the method has been well developed and applied to industry for 200 years and continues to modern time.

Compared to e-beam evaporation deposition, the advantages of sputtering deposition are the following: capability to deposit and sustain complex alloys, ability

to deposit high-temperature and refractory metals, and get higher energy atoms, smaller grain size, and better adhesion.

The main operation begins with filling the vacuum chamber with a argon. A significant aspect of sputtering is the transformation of the ionized argon gas into plasma. When a high voltage is applied to the vacuum chamber, the argon will arc to the plasma state. Argon is relatively heavy and is a chemically inert gas so it acts as the ion species for the sputtering process. Argon gas also does not react with the growing film or the target.

When a high-energy electron ranging from 500 to 5,000 eV hits the neutral argon, outer electrons and a positively charged argon ion are separated by the collision. This energetic particle is used to strike the negatively charged target material to be sputtered. When the positive argon ions hit the surface of the target material, the momentum of the argon ion transfers to the target material to dislodge one or more atoms. This process is based on momentum transfer. The positively charged argon ions will move to the negative potential of cathode with high speed as they pass through the voltage drop of the glow-discharge dark space. The target atom or molecule will attach to the substrate surface and condense as a film.

The target atom is knocked out by the positive argon ion. The knock force is great and can accelerate the target atom to a high speed. With such velocity, the target atom can strike and attach to the surface of the wafer substrate deeply, so the sputtered film density is better than the evaporation film density. Figure 3.3 shows the image of sputtering process.

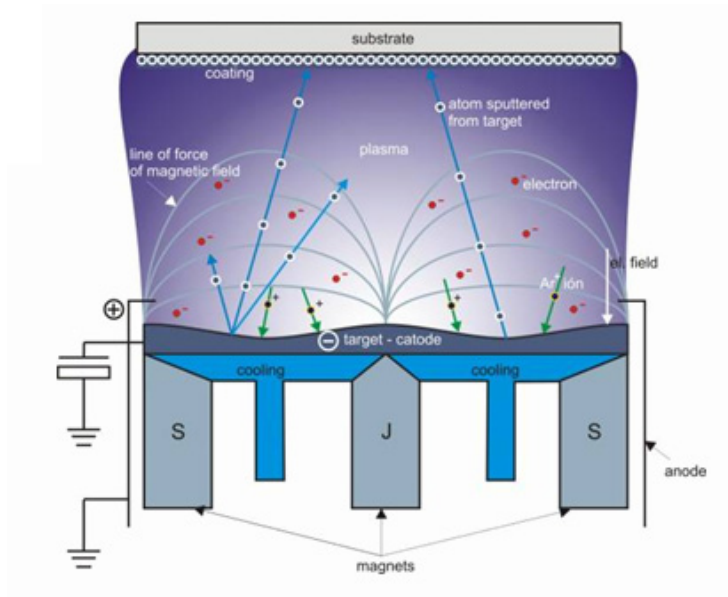


Figure 3.3 Image of sputtering process[35].

In this experiment, DC sputtering is used for deposition of CoFeB islands. Magnets placed around and behind the material target are used in order to capture and restrict the electrons. The ion bombardment rate of the target increases with the creation of more secondary electrons, which then also increases the ionization rate during the plasma formation. As a result, more ions lead to more sputtering of the target, which develops the deposition rate. The magnetron sputtering is developed for improved deposition rate, which explains why sputtering has become the principal process for aluminum and contact alloys used in metallization.

At first, the sample finished by e-beam patterning is transferred through the loading chamber into the high vacuum deposition chamber. For the sputtering process, the base pressure is 5.5 mTorr and the operation power is set up to 69 watt for a stable process. The deposition time is determined by the desired CoFeB film thickness with various times of 1 minute, 2 minutes, 3 minutes, 5 minutes, 7 minutes,

9 minutes, 12 minutes, and 15 minutes. With the operation power set to 69 watts for a stable sputtering process, the deposition rate is about 6.5 nanometers per minute.

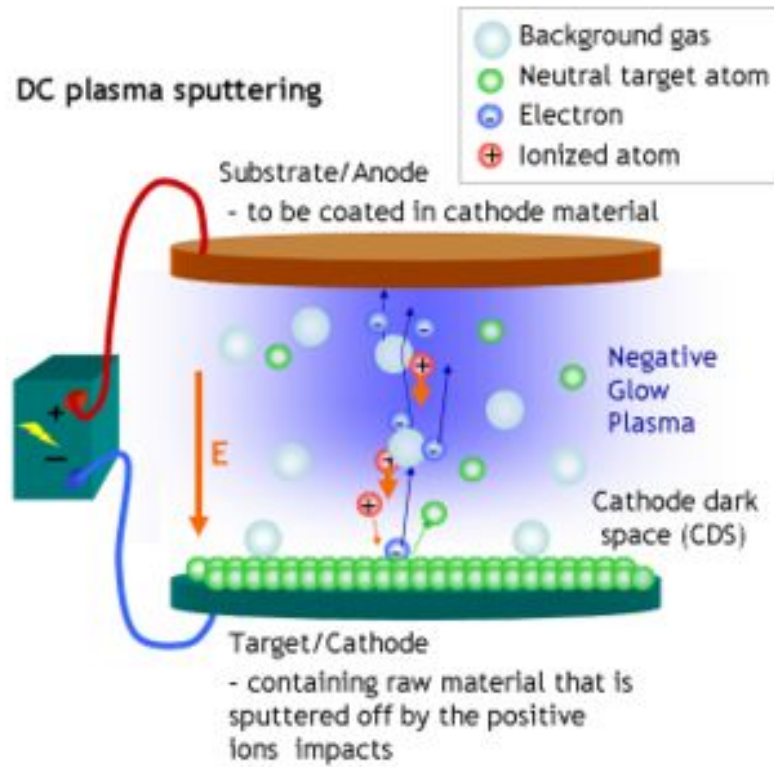


Figure 3.4 DC Sputtering process[36].

### 3.4. Lift-off

Lift-off is the process to directly make a pattern of the ferromagnetic material by using a solvent to dissolve the remaining e-beam resist underneath the ferromagnetic material. The process sequence is comparable to the normal photolithography process. The process is summarized in figure 3.5.

For positive e-beam resist like PMMA 495/950, after the substrate has been exposed, another step is performed to create the desired overhanging profile necessary for lift-off. The ferromagnetic material like CoFeB is deposited onto the substrate. Once the e-beam resist is removed, the ferromagnetic material covering the e-beam resist is also removed (lifted off). Sometimes the ultrasonic bath and slight mechanical scrubbing with a clean room swab is necessary for assistance in the lift-off process.

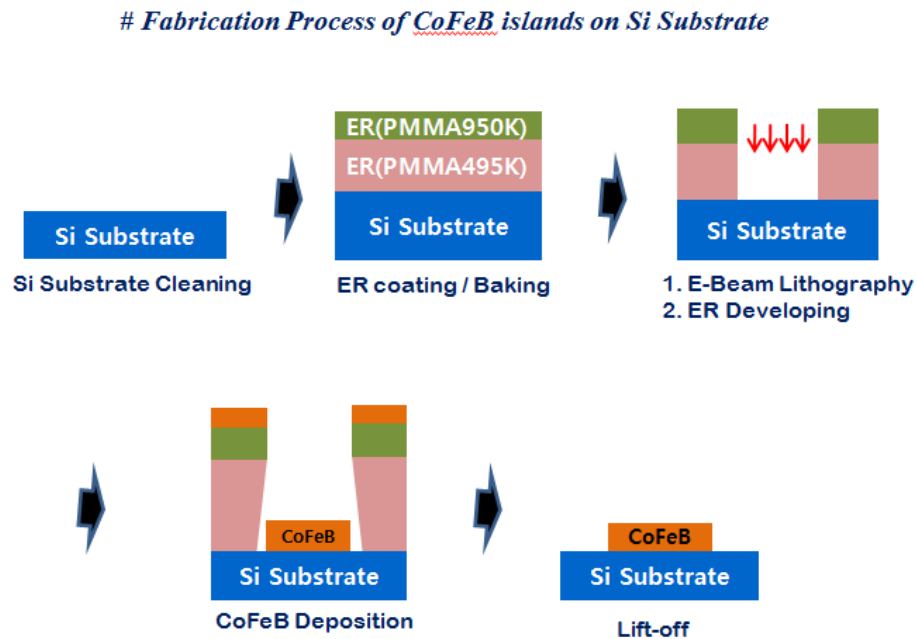


Figure 3.5 Lift-off process.

### 3.5 Annealing

The ferromagnetic films deposited by the sputtering process are generally not in saturated equilibrium and under residual stress. This is removed by moderate annealing. The samples are annealed in an ultra-high vacuum (UHV) chamber by direct resistance heating. The samples are annealed in an ultra-high vacuum (UHV) chamber by direct resistance heating. The base pressure of the UHV chamber is  $3 \times 10^{-9}$  mTorr, with the maximum attainable temperature of 400 °C. During the annealing, samples are gently placed on 20 mm × 20 mm Tantalum plate which is connected to the heating filament. The annealing is performed at the constant temperature of 400 °C for 1 hour. Figure 3.6 shows the total experiment process from sample preparation to MFM measurement.

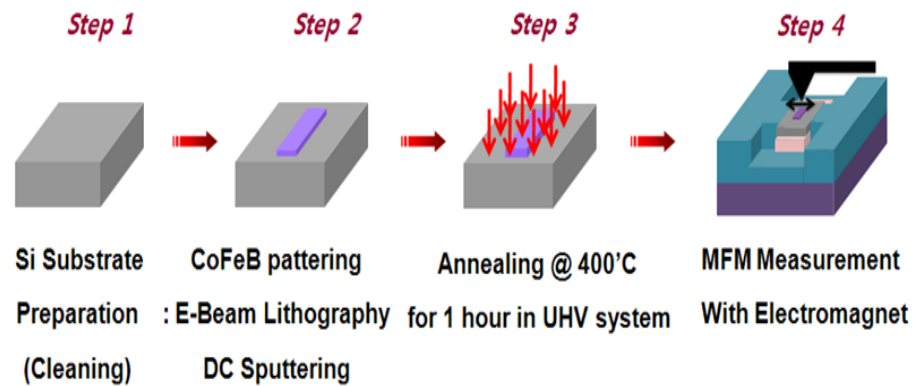


Figure 3.6 Experiment process from sample preparation to MFM measurement.

## **3.6 Magnetic force microscopy (MFM)**

### **3.6.1 Introduction**

For observation of magnetic domain images of ferromagnets like Ni, Co, and Fe, magnetic force microscopy (MFM) has been one of the most extensively utilized tools because commercial MFMs have been relatively inexpensive and the sample can be imaged without any special preparation. A combination of those reasons with sub-micron resolution capabilities has made MFM useful for magnetic images[37][38][39].

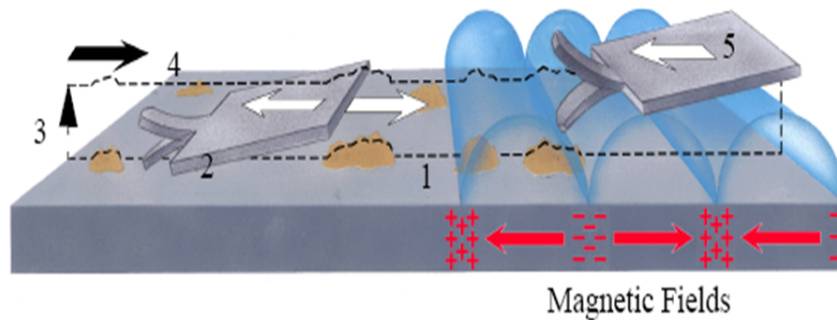
In this experiment, a Multi-Mode MFM with a Nanoscope III controller, both from Digital Instruments, was used. The probe used was also purchased from DIGITAL Instruments. The probes are etched silicon with a magnetic material. In this case cobalt-chromium is deposited on the very end of a cone shape apex to provide the magnetic interaction.

A magnetic tip coated with 20nm thick cobalt-chromium film is pre-magnetized upward along the tip axis and used to scan in a tapping-lift mode. An especially low moment probe is used at a lift height of 60nm to minimize the measurement-induced domain wall motion[40][41].

### **3.6.2 Principle of operation**

Figure 3.7 shows the principles of MFM *Lift* modes. The basic principal of operation of MFM equipment for obtaining magnetic images is explained with the following steps : First, in *tapping* mode, a cantilever attached to a special magnetized AFM tip is first scanned to profile the topographic information of the sample surface.

Next, in *Lift* mode, the tip is forced to retrace the topography of the sample surface by the influence of magnetic fields from a set distance above the surface. Lastly, those influences between the applied magnetic field and the magnetized AFM tip are measured by force gradient detection for producing a magnetic image. Figure 3.7 explains the main principles of MFM Lift modes.



1. Cantilever traces surface topography on the first trace.
2. Cantilever retraces surface topography on the first retrace.
3. Cantilever ascends to Lift scan height.
4. Lifted cantilever profiles topography while responding to magnetic influences on the second trace.
5. Lifted cantilever profiles topography while responding to magnetic influences on the second retrace.

Figure 3.7 Principles of MFM Lift modes.

During the operation, the cantilever is forced to oscillate at its resonant frequency by a set of piezoelectric bimorphs. The resonant frequency is controlled by a tuning process of the Digital Instruments software. The sample was moved beneath the MFM tip by other piezoelectrics in order for to the tip to raster over a rectangular area of the sample. While the tip gets close to the sample surface, a change in oscillation occurs due to the magnetic interaction between the tip and the sample. The variation of oscillation is observed by a photo-detector placed in the scanning head of the MFM. A light is bounced off the back of cantilever and is detected by a photo-

detector. The light beam is directed at the portion of the cantilever directly on the other side of the tip to give the maximum deflection. The deflection is processed by a series of steps into the images created by the MFM. Figure 3.8 shows the schematic of the MFM.

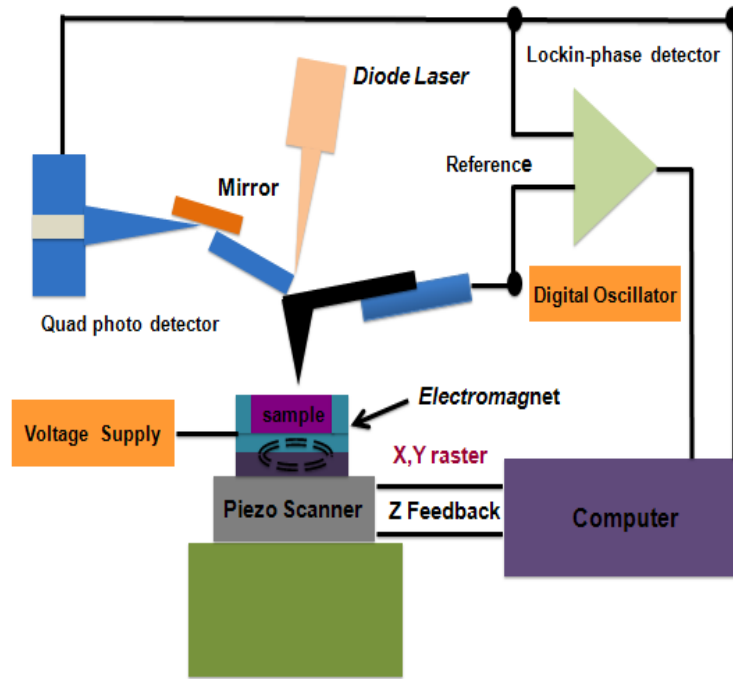


Figure 3.8 Schematic diagram of MFM implementation.

It is possible to obtain information of magnetic interaction by phase detection, which measures the cantilever's phase of oscillation relative to the piezo drive. In phase detection, the tip is used as a damped forced harmonic oscillator. This approximation is valid since the oscillation amplitude is small relative to the length of the cantilever and tip to consider the displacement to be only in the vertical direction. The equation related to the change in phase of oscillation with the force derivative of the tip can be expressed as the following[42][43] :

$$\Delta \Phi \approx \frac{-Q\partial f_z}{mW_r^2\partial z}(x, y, z_0) \quad (3.1)$$

In equation 3.1,  $m$  is the mass of the tip,  $W_r$  is the resonant frequency, and  $Q$  is the quality factor. Also,  $Q$  is affected by the damping coefficient,  $b$ .

$$Q = \frac{mW_r}{b} \quad (3.2)$$

However the relation between the force derivative and the stray fields from the sample still needs to be considered. For this consideration, the probe is modeled as a magnetic dipole with moment  $m$  located where the tip is.

The following equation 3.3 expresses the relations between the force gradient and the stray fields from the sample.

$$\frac{\partial F_z}{\partial z} = m_x \frac{\partial^2 B_x}{\partial z^2} + m_y \frac{\partial^2 B_y}{\partial z^2} + m_z \frac{\partial^2 B_z}{\partial z^2} \quad (3.3)$$

However, in practice, the vector surface magnetization from the scalar data generated by the MFM is difficult to determine exactly.

## 3.7 Applying in-plane magnetic field with an electromagnet

### 3.7.1 Electromagnet

It is significant to investigate the change of magnetic domains with externally applied magnetic fields, so an electromagnet is very useful in this experiment. The electromagnet was placed on the stage of the MFM and the sample was then placed so that the surface of the array was flush with the top surface of the electromagnet. Figure 3.9 shows a schematic of an electromagnet with a cooling system. In this electromagnet, a permeable “C” shape core with a winding of thin magnet wire is a very significant part.

The necessary magnetic field is induced by the core and coil device. The core is chosen to be a permalloy alloy material for obtaining a high permeability. Thin wire has an advantage considering the high number of turns for limited space, but it reduces the maximum current. The magnetic field generated in the gap of length  $L_g$  can be estimated[43]

$$B_g = U_g \times NI / L_g, \quad (3.4)$$

Where  $N$  is the total number of turns,  $I$  is the current through the coil, and  $U_g$  is the permeability of free space. Equation 3.4 is derived from Ampere’s law and assumes that the permeability of permalloy is much larger than the permeability in free space. High currents necessary for high field produce substantial resistive heat which cause the thermal drift of the magnetic field image and alter the magnetic property of the sample.

For this reason, a thermo-electric cooler and water-cooling line was incorporated into the design as shown in Figure 3.9. The larger copper block is also used as a heat sink. The thermo-electric cooler delivers the heat from the electromagnet to the copper block and chilled water driven by a mechanical motor flows through the line inside the copper block. This electromagnet system generates 3 kOe without serious thermal effects.

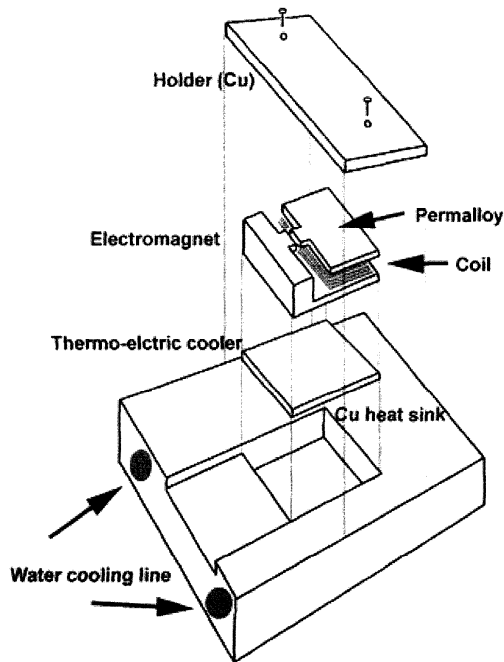


Figure 3.9 Schematic diagram of an electromagnet with a cooling system.

For calibration of the applied voltage and the measured magnetization, the electromagnet and a gauss-meter are used. The Hall probe is placed in the gap of the electromagnet so that the gap holes of the magnet were parallel to the face of the probe. The electromagnet was then connected to a Keithley 220 Programmable

Voltage Source and the magnetic fields were measured as a function of voltages. While the voltage is applied from 0V to  $\pm 10$ Volts, the magnetic fields were measured. This electromagnet system generates 3 kOe without serious thermal effects, but in this experiment, the magnetic fields were applied with the range from 0 Oe to  $\pm 1,000$  Oe for a stable thermal state. Table 3.1 and 3.2 shows the calibration between applied voltages( $\pm$ ) and measured magnetic flux density( $\pm$ ).

Voltage (+V)	Magnetization (-G)	Voltage (V+)	Magnetization (+G)	Voltage (+V)	Magnetization (+G)	Voltage (+V)	Magnetization (+G)
0	1.2	10.5	747	30	1581	9.5	675
0.5	36.6	11	783	20	1265	9	641
1	73.6	11.5	816	19	1250	8.5	605
1.5	110	12	846	18.5	1203	8	574
2	147	12.5	880	18	1183	7.5	541
2.5	185	13	911	17.5	1159	7	504
3	220	13.5	944	17	1133	6.5	471
3.5	257	14	976	16.5	1108	6	437
4	292	14.5	1008	16	1075	5.5	403
4.5	328	15	1039	15.5	1048	5	367
5	365	15.5	1065	15	1019	4.5	332
5.5	400	16	1099	14.5	991	4	298
6	437	16.5	1123	14	961	3.5	262
6.5	471	17	1152	13.5	932	3	226
7	508	17.5	1179	13	896	2.5	191
7.5	541	18	1207	12.5	868	2	156
8	578	18.5	1233	12	836	1.5	120
8.5	612	19	1259	11.5	803	1	84
9	646	20	1312	11	771	0.5	48
9.5	680	30	1615	10.5	738	0	11.2
10	715	39	1706	10	706		

Table 3.1 Calibration data of applied voltages(+) and measured magnetization(+).

Voltage (-V)	Magnetization (-G)	Voltage (-V)	Magnetization (-G)	Voltage (-V)	Magnetization (-G)
0	1.2	10.5	726	10	637
0.5	25.3	11	765	9	594
1	61.4	11.5	828	8	545
1.5	98.2	12	860	7	487
2	134	12.5	878	6	422
2.5	170	13	891	5	356
3	208	13.5	922	4	286
3.5	242	14	948	3	218
4	281	14.5	978	2	147
4.5	315	15	1014	1	75.7
5	350	20	1297	0	4.8
5.5	386	25	1500		
6	420				
6.5	456				
7	490				
7.5	525				
8	560				
8.5	595				
9	630				
9.5	662				
10	695				

Table 3.2 Calibration data of applied voltages(-) and measured magnetization(-).

### 3.7.2 Applying magnetic field to the sample.

In order to apply in-plane magnetic field in the gap between the electromagnets, the sample is diced into 2mm x 10mm pieces and an electromagnet with a cooling system was used with the applied voltage range from 0V to +4.5/-3.5V.

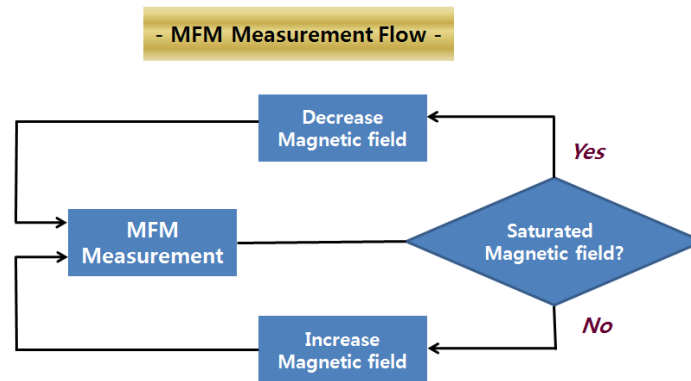


Figure 3.10 Flow process of MFM measurement with electromagnet.

Figure 3.10 explains the MFM measurement flow of the CoFeB pattern. As the magnetic field is applied to the sample by the electromagnet through a voltage supplied with increments of 0.5V, MFM measurements are performed in order to observe the change of the magnetic domain with magnetic vortex-antivortex pairs. If the applied magnetic fields saturate the sample, when there exist no magnetic features, the magnetic field is decreased until the magnetic field arrives at the opposite saturated state. In the following chapter 4, several MFM images of 50nm thick CoFeB patterns under different applied voltages are shown to study the creation and annihilation of vortex-antivortex pairs.

## Chapter 4. Results and discussion

### 4.1 Magnetic domains into 7 categories.

Generally, magnetic domain configurations are classified into seven types of domain configurations. The seven domain configurations are divided into two categories: solenoidal and non-solenoidal. In the case of solenoidal domains, closure loops are created within the overall island with zero net magnetization. A non-solenoidal domain configuration has a net magnetization resulting from free poles so the magnetization does not create closed loops within the pattern.

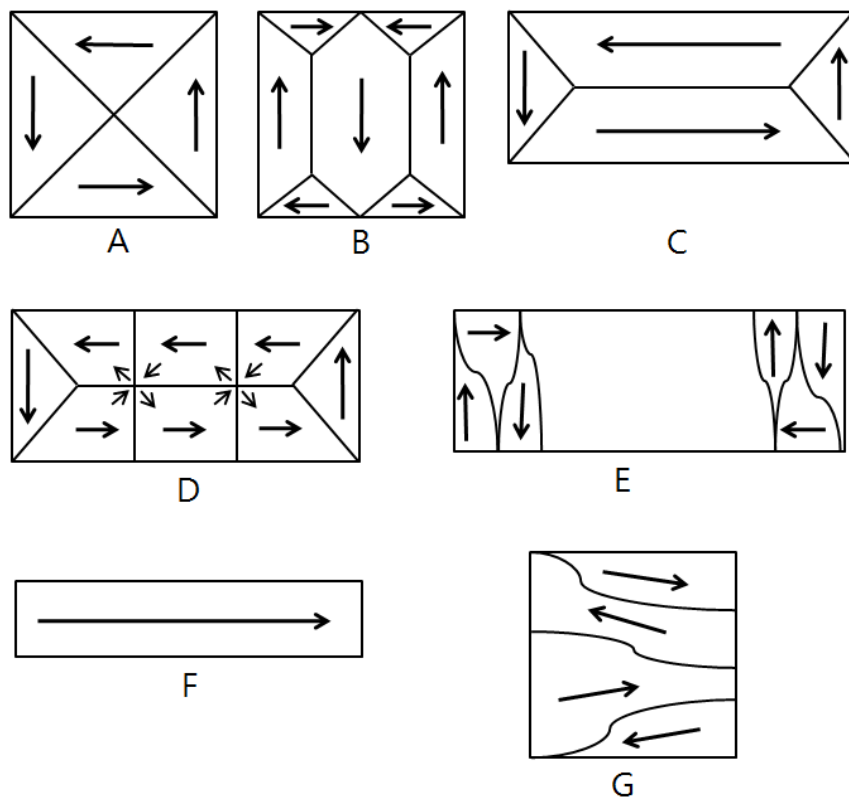


Figure 4.1 Seven types of magnetic domain configurations.

The following types A through D are the domain patterns of the solenoidal configurations. Type A is a four-domain closure pattern with  $90^\circ$  walls separating the domains and is usually observed in square patterns. The magnetizations of neighboring domains are perpendicular to one another.

Type B is a seven-domain closure pattern with a mixture of  $90^\circ$  and  $180^\circ$  walls that removes free poles. The well-defined seven domains show the aspect ratio of nearly two between the length and the width of the domains. This pattern is sometimes observed in the intermediate state between a non-solenoidal and solenoidal state. In this domain, there exist some interior vertices, a core of a vortex, which creates a closure loop due to in-plane magnetization.

Type C is a four-domain closure pattern with both four  $90^\circ$  walls and a  $180^\circ$  wall. This could be a modified type A configuration of which top and bottom domains are lengthened compared to the side domains. So, in the top and bottom domains, the magnetization is anti-parallel with one another, but in the left and right end domains the magnetizations are perpendicular to the top and bottom domains. The line dividing the top and bottom domains is a  $180^\circ$  wall. This is commonly found in a pattern whose aspect ratio is near two.

Type D is a variation of type C with cross-ties and Bloch lines included along the  $180^\circ$  wall. As the cross-tie wall exists in the boundary between the top and bottom domains, the magnetostatic energy of the  $180^\circ$  wall is reduced. In the case of a high aspect ratio between the length and the width, several cross-ties in one  $180^\circ$  wall are likely to be generated.

The other types of domain configurations are all non-solenoidal. Type E formation is a quasi-single domain with closure ends. In this pattern the remanent state of the interior region is always magnetized along the long axis. However, breaking up both ends into smaller closure domains lowers the magnetostatic energy involved with having free poles at the ends. In these domains, perfect closure patterns cannot be created, but free magnetic charges at the edges of the pattern are removed. The MFM image of this pattern shows a bright distinction at one closure end and dark at the other with a constant magnetization in the middle of the pattern. At both of the ends, individual domain walls can be observed making the edge structure.

Type F is a variation of type E like a true single domain. In this case, the pattern is also magnetized along its long axis but the end structures cannot be resolved. The MFM images of this domain type show the domain to be dark at one end and bright at the other with no comparison in the middle area. This domain pattern shows no domain walls and is usually observed in very narrow islands. The next chapter will explain the requirement for the formation of a single domain.

Type G is a complex type of non-solenoidal multi-domain configuration with curved domain walls within the pattern. In this pattern, the magnetization is usually shown by a dark contrast at the top and bright at the bottom or vice versa. This domain configuration is complicated with no apparent regularity. It does not have a well-defined arrangement of domain walls. When an external magnetic field is applied to the various islands, MFM images of the islands have continuously shown this pattern is reproducible. This pattern is the preferred domain configuration for large islands when saturated with an applied magnetic field. The presence of the

curved walls in this island may result in induced uniaxial anisotropy of the islands, so the creation of domains oriented perpendicular to this axis would be energetically costly, which explains why the type G has a predominance in the large islands. The size of the domain becomes too large and the cost of maintaining a domain of that size is energetically very expensive so the islands would break up into more domains.

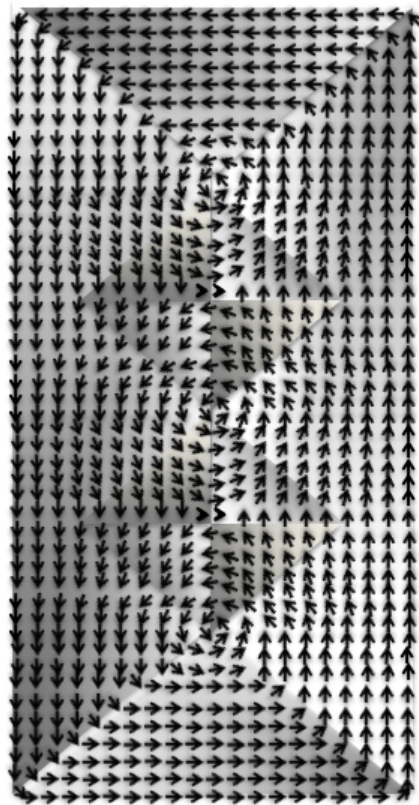
## **4.2 Interpretation of the MFM images with the aid of micromagnetic modeling**

The magnetic structure of cross-tie walls observed in magnetic thin films is one of the most attractive structures for the study of vortices, since it includes two types of magnetic vortex structures: a defined vortex and an antivortex. It has been possible to use the classic theories of magnetism to model the domains of small elements with advanced computers. Smyth et al. have investigated the effects of particle size, aspect ratio, and interparticle spacing on the hysteretic properties of the ensemble and compared them with calculations[44]. Zhe et al. has shown that their modeling of the micro-magnetic behavior of exchange biased ten micron patterns is in good agreement with experimental observation.[45] Schrefl et al. have studied the effects of edge geometry on the switching dynamics of submicron Permalloy elements[46].

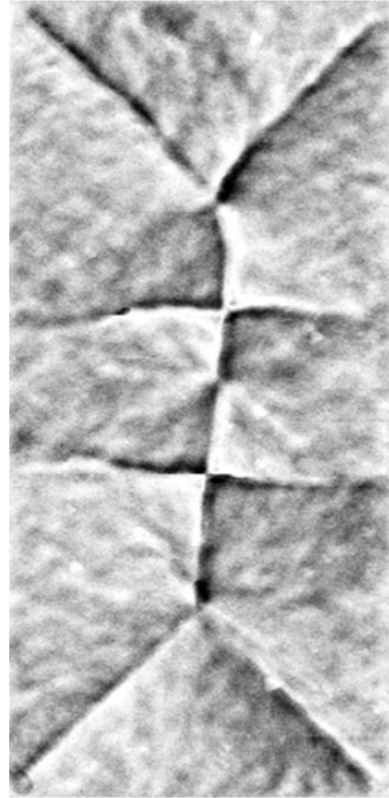
Since it is possible to obtain information about magnetic divergence and not information about the magnetization itself by MFM images, micro-magnetic modeling work is useful in the modeling of micron and submicron sized CoFeB patterns. The divergence plots from the Objected Oriented Micro Magnetic Framework (OOMMF) program, developed by National Institute of Standards and

Technology (NIST) can be utilized as a check against the MFM data to assure that the classifications of the walls are indeed the correct ones. As shown in figure 4.2, micro-modeling(left) and MFM(right) images of a rectangular CoFeB island of  $16\ \mu\text{m} \times 8\ \mu\text{m}$  at remanent state describe the existence of two cross-tie structures with a magnetic vortex between them. The left image shows especially the distribution of the magnetization  $\vec{M}$  for the cross-tie wall. The equilibrium magnetization is found by solving the dynamic Landau–Lifshitz–Gilbert equation. Only the magnetostatic energy and the exchange energy are considered.

The magnetization is also expressed by the arrows while the divergence is shown by the shaded regions. This pattern also has four  $90^\circ$  domain walls starting from all corners of the pattern. Apparently, it shows that the magnetizations of the domain separated by the walls are perpendicular to one another. At the cores of the vortex and antivortex, the existence of a spot with perpendicular magnetization has been theoretically predicted. In the vicinity of the vortex core, the angle between adjacent spins would become increasingly larger if the spin directions were confined in-plane. Therefore, at the core of the vortex structure, the magnetization within a small region will turn out-of-plane not to increase the exchange energy. Analyzing these figures, it is possible to confidently identify the types of domain walls and structures in the MFM data.



Magnetization Pattern



MFM Image

Figure 4.2 Magnetization pattern (Left) and MFM image(right) of a rectangular island with the size of  $16\mu\text{m} \times 8\mu\text{m}$ .

### 4.3 Magnetic domain configurations with different thicknesses

From figure 4.3 to figure 4.10, MFM images of CoFeB islands with different thicknesses islands are shown. In all MFM images, each pattern is first classified according to the type of magnetic domain, referred in the previous section 4.1 and is marked with the micron dimensions.

Figure 4.3 shows the MFM image of 7 nm thick CoFeB islands with different sizes from 250 nm to 16  $\mu\text{m}$ . The CoFeB film is too thin such that no magnetic features like magnetic domain wall or magnetic vortex are observed in the MFM image.

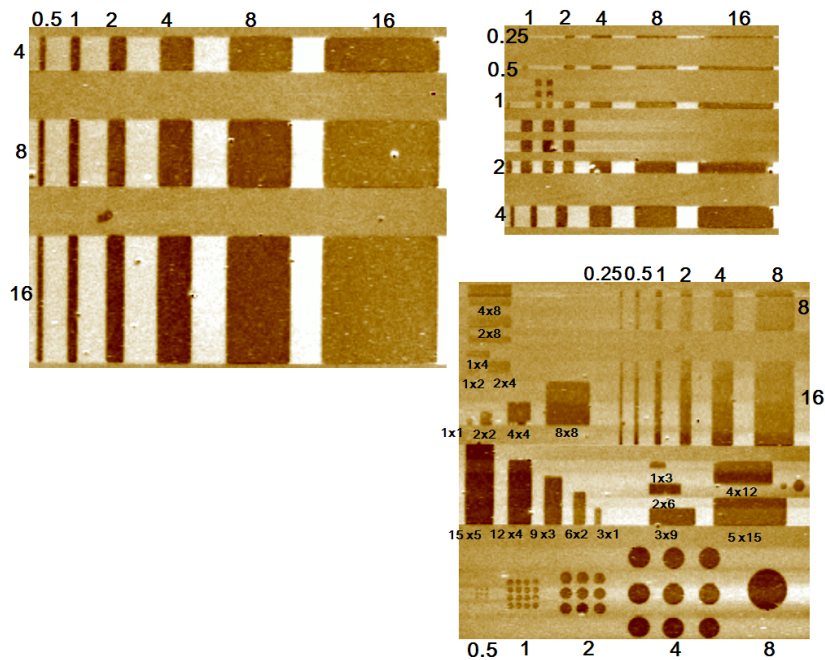


Figure 4.3 MFM images of CoFeB islands with 7 nm thickness.

Figure 4.4 shows the MFM image of 13 nm thick CoFeB islands with different sizes from 250 nm to 16  $\mu\text{m}$ . As the thickness increases, magnetic domains appear. Especially in the CoFeB islands of the size 16 $\mu\text{m}$  x 8 $\mu\text{m}$  and 16 $\mu\text{m}$  x 4 $\mu\text{m}$ , 4-domains or 7 domains are observed. Also, in the circles of CoFeB pattern, magnetic features like a magnetic vortex or an antivortex are found.

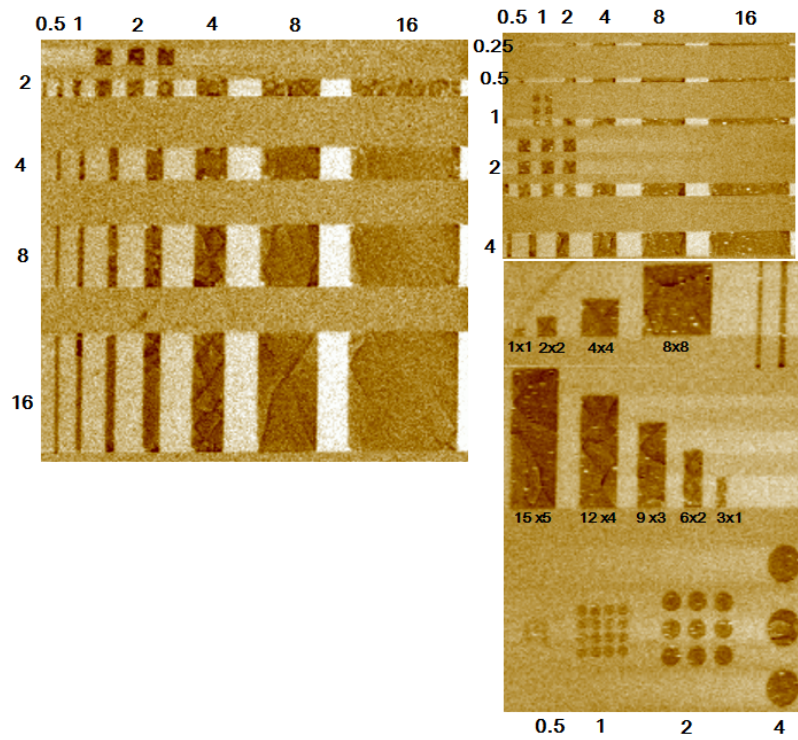


Figure 4.4 MFM images of CoFeB islands with 13m thickness.

Figure 4.5 shows the MFM image of 19 nm thick CoFeB islands with different sizes from 250 nm to 16  $\mu\text{m}$ . In the square patterns of 1  $\mu\text{m}$  x 1  $\mu\text{m}$ , 2  $\mu\text{m}$  x 2  $\mu\text{m}$ , 4  $\mu\text{m}$  x 4  $\mu\text{m}$  and 8  $\mu\text{m}$  x 8  $\mu\text{m}$ , 4-domain structures with a 90° domain wall are observed and in 4  $\mu\text{m}$  x 16  $\mu\text{m}$ , 5  $\mu\text{m}$  x 15  $\mu\text{m}$ , and 4  $\mu\text{m}$  x 12  $\mu\text{m}$  islands, 7-domain structures with a 2 or 3 aspect-ratio between the length and width are found. In other patterns with the aspect ratio higher than 8, usually a single domain with uniform magnetization is formed, but 4-domain structures with cross-tie walls are still not found.

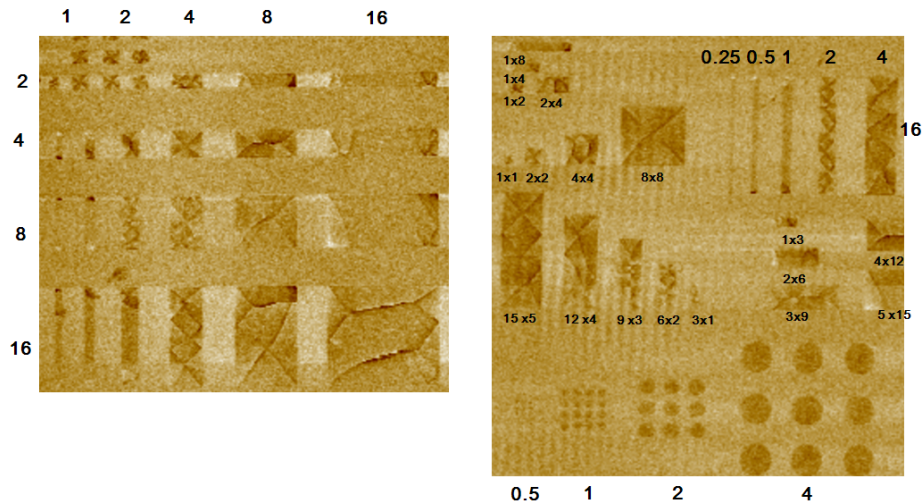


Figure 4.5 MFM images of CoFeB islands with 19nm thickness.

Figure 4.6 shows the MFM image of 28 nm thick CoFeB islands with different sizes from 250 nm to 16  $\mu\text{m}$ . In the rectangular pattern of 8  $\mu\text{m}$  x 16  $\mu\text{m}$ , a cross-tie domain with a magnetic vortex is observed. Also in the patterns with aspect-ratios of 2 or 4, magnetic domains are seen much clearer than in the previous thin film. However, in the circle pattern, a magnetic vortex or antivortex is still not found clearly.

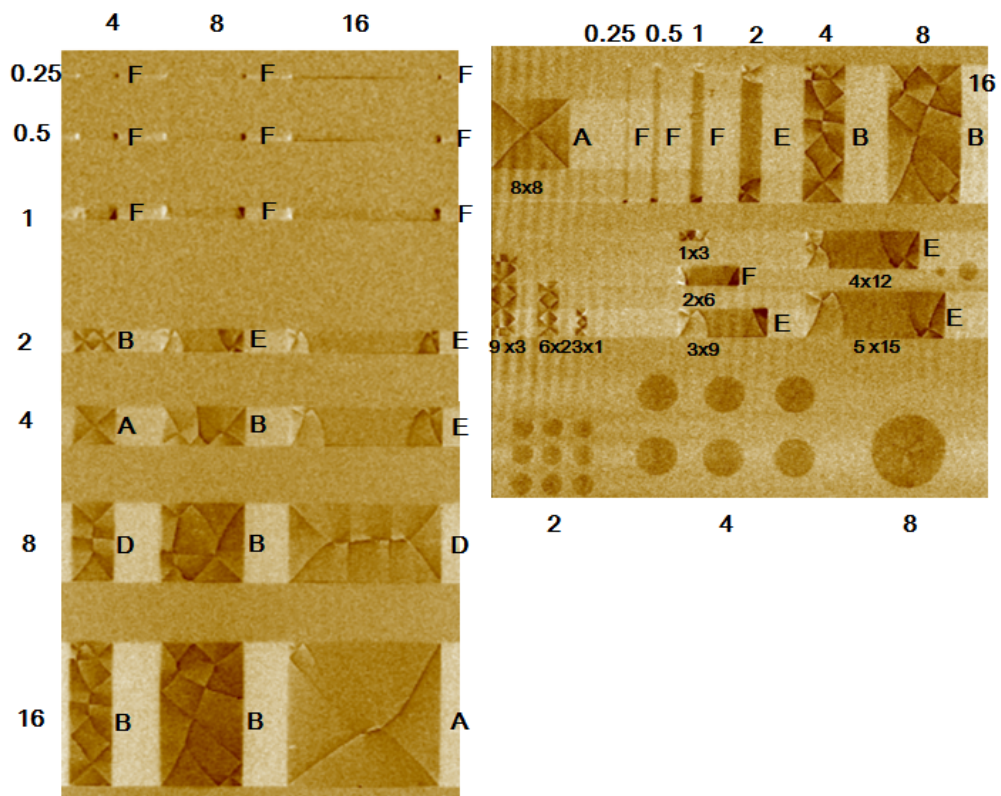


Figure 4.6 MFM images of CoFeB islands with 28nm thickness.

Figure 4.7 shows the MFM image of 37 nm thick CoFeB islands with different sizes from 250 nm to 16  $\mu\text{m}$ . As shown in figure, the devices of 2 $\mu\text{m}$  x 4 $\mu\text{m}$ , 4 $\mu\text{m}$  x 2 $\mu\text{m}$ , 4 $\mu\text{m}$  x 16 $\mu\text{m}$ , 8 $\mu\text{m}$  x 4 $\mu\text{m}$ , 8 $\mu\text{m}$  x 2 $\mu\text{m}$ , and 8 $\mu\text{m}$  x 16 $\mu\text{m}$  have a cross-tie domain wall with a vortex-antivortex pair. Interestingly, in the case of the circular pattern with 4 and 8  $\mu\text{m}$  diameters, it shows a single magnetic domain. Similar to the previous figure 4.1, square patterns have a 90° domain structure. Islands with an aspect ratio larger than 8 show a single domain as the domain structure.

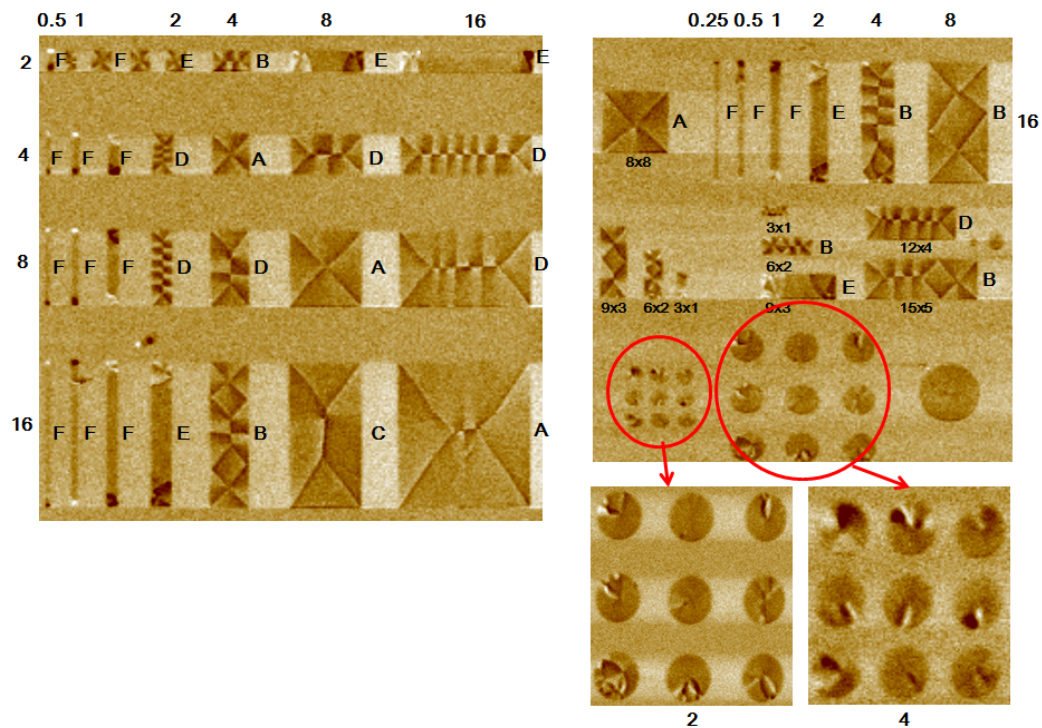


Figure 4.7 MFM images of CoFeB islands with 37nm thickness.

Figure 4.8 shows the MFM image of 45 nm thick CoFeB islands with different sizes from 250 nm to 16  $\mu\text{m}$ . Still, the square patterns of 1  $\mu\text{m}$  x 1  $\mu\text{m}$ , 2  $\mu\text{m}$  x 2  $\mu\text{m}$ , 4  $\mu\text{m}$  x 4  $\mu\text{m}$  and 8  $\mu\text{m}$  x 8  $\mu\text{m}$ , show the 4-domain structure with 90° domain wall. The domain structure of other islands, including 8  $\mu\text{m}$  x 8  $\mu\text{m}$ -square and 8  $\mu\text{m}$  x 16  $\mu\text{m}$ , 4  $\mu\text{m}$  x 16  $\mu\text{m}$  and 4  $\mu\text{m}$  x 8  $\mu\text{m}$  rectangular patterns became complicated, much as a 4-domain structure changes to a 7-domain structure. In the case of the 8  $\mu\text{m}$  x 16  $\mu\text{m}$  rectangular pattern, the number of cross-tie walls increased compared to the thinner same sized pattern. In the circular patterns of 4  $\mu\text{m}$  x 4  $\mu\text{m}$ , a magnetic vortex is not clearly observed.

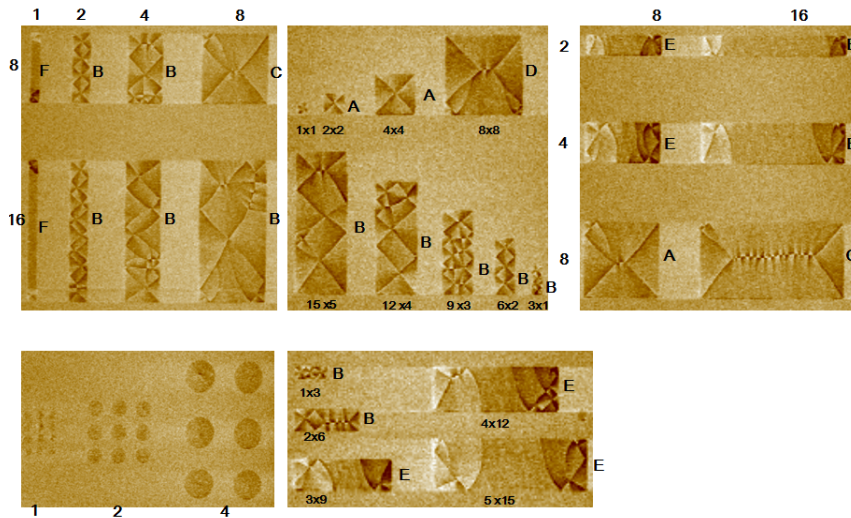


Figure 4.8 MFM images of CoFeB islands with 45nm thickness.

Figure 4.9 shows the MFM image of 52 nm thick CoFeB islands with different sizes from 250 nm to 16  $\mu\text{m}$ . Interestingly, 8  $\mu\text{m}$  x 8  $\mu\text{m}$  and 4  $\mu\text{m}$  x 4  $\mu\text{m}$  square patterns (left) became much more complicated, changing from a 4-domain to a 7-domain structure with two cross-tie walls. Patterns with a 3 aspect-ratio show a 4-domain structure with a magnetic vortex-antivortex pair. However, in the case of the circular patterns, no magnetic features are shown.

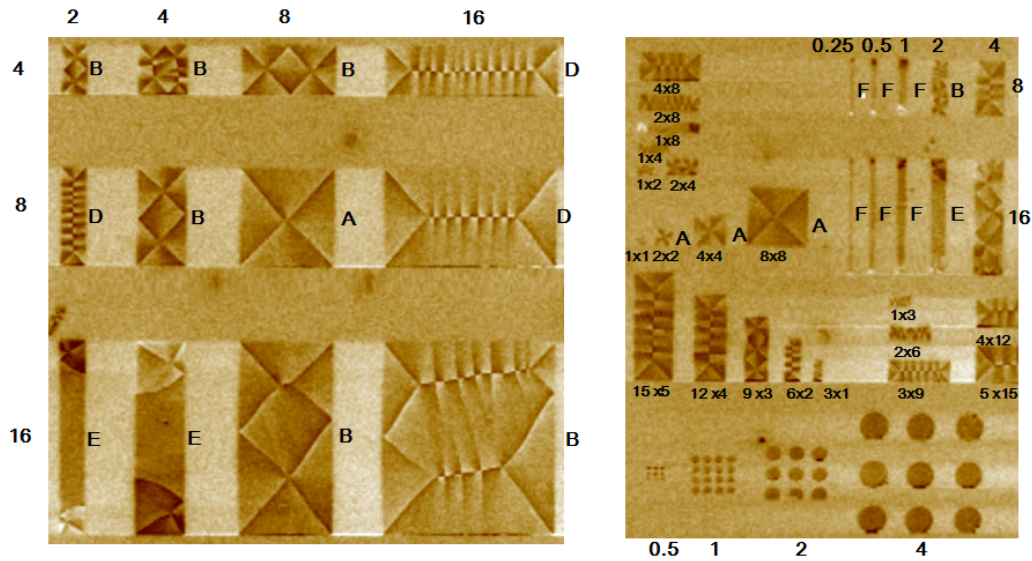


Figure 4.9 MFM images of CoFeB islands with 52nm thickness.

Figure 4.10 shows the MFM image of 63 nm thick CoFeB islands with different sizes from 250 nm to 16  $\mu\text{m}$ . Most patterns with 2, 4 and 8 aspect ratios became much more complicated with more cross-tie walls. In the case of the islands with an aspect ratio of 3, MFM images show the combination of a 7-domain and a 4-domain structure with a magnetic vortex-antivortex pair. In the patterns with an aspect ratio higher than 8, a single domain structure is observed.

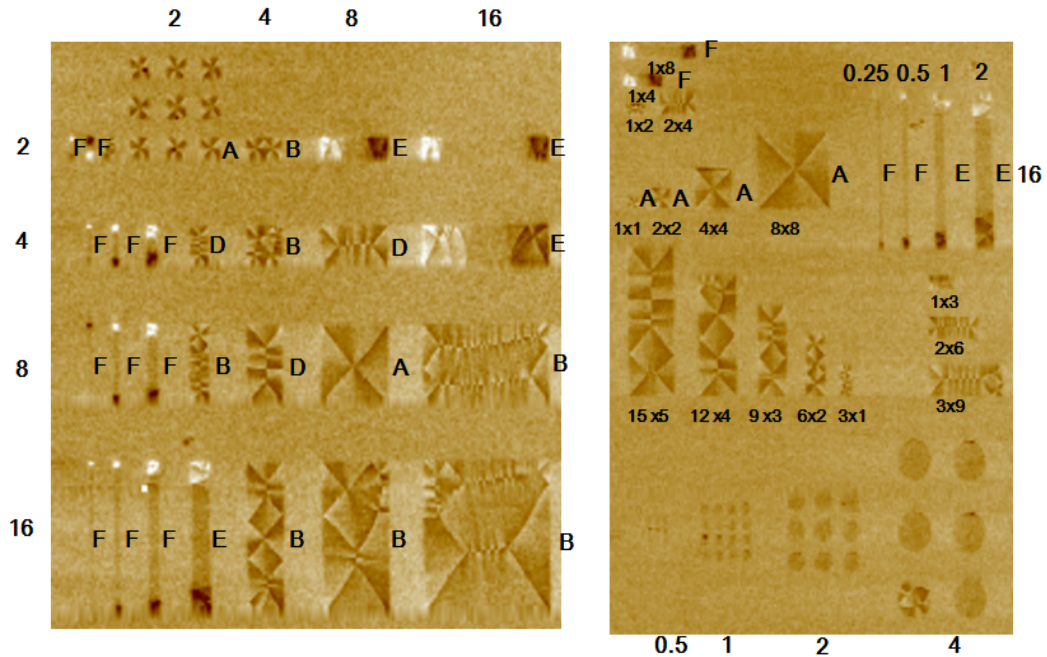


Figure 4.10 MFM images of CoFeB islands with 63nm thickness.

Lastly, figure 4.11 summarizes the MFM images with different thicknesses of CoFeB film, focusing on the 9 patterns with the size of  $4\mu\text{m} \times 4\mu\text{m}$ ,  $4\mu\text{m} \times 8\mu\text{m}$ ,  $4\mu\text{m} \times 16\mu\text{m}$ ,  $8\mu\text{m} \times 4\mu\text{m}$ ,  $8\mu\text{m} \times 8\mu\text{m}$ ,  $8\mu\text{m} \times 16\mu\text{m}$ ,  $16\mu\text{m} \times 4\mu\text{m}$ ,  $16\mu\text{m} \times 8\mu\text{m}$ , and  $16\mu\text{m} \times 16\mu\text{m}$ . The thickness of CoFeB patterns varies from 7 nm, 13nm, 19nm, 28nm, 37nm, 45nm, 52nm to 63nm. In the case of two patterns,  $8\mu\text{m} \times 16\mu\text{m}$  and  $16\mu\text{m} \times 16\mu\text{m}$ , magnetic domains are created and the number of magnetic vortex-antivortex in cross-tie walls increases as the thickness of CoFeB film increases, except for the 45 nm thickness. Square patterns like  $4\mu\text{m} \times 4\mu\text{m}$ ,  $8\mu\text{m} \times 8\mu\text{m}$ , and  $16\mu\text{m} \times 16\mu\text{m}$  appear to form a 4-domain structure with  $90^\circ$  domain wall as the CoFeB film thickness increases, except for the 28 nm thickness. MFM images of the

16 $\mu\text{m}$  x 4 $\mu\text{m}$  rectangular pattern shows the complicated structure of the combination of a 4-domain and a 7-domain structure.

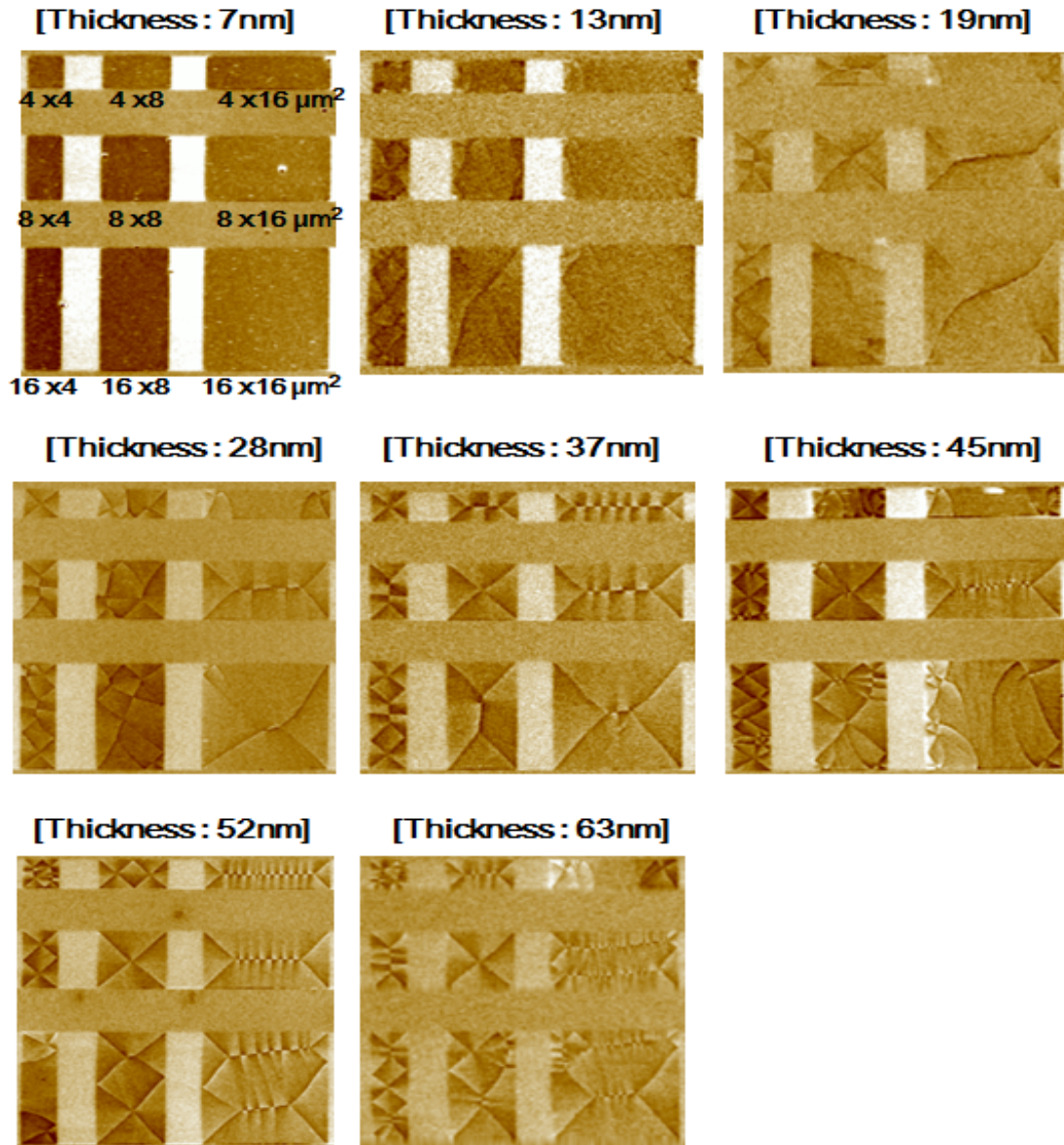


Figure 4.11 MFM images of CoFeB islands with different thickness.

Quite generally but with some exceptions, the trend on all patterns is the increase in the number of vortex-antivortex pairs as a function of thickness. The reason is that the Néel wall energy increases with thickness, making it energetically more favorable to create crosstie walls.

#### **4.4 Vortex–antivortex creation and annihilation in CoFeB patterns with a cross-tie wall**

The previous section showed several types of magnetic domain structures. Out of several CoFeB patterns, the pattern of size  $16\mu\text{m} \times 4\mu\text{m}$  is chosen in order to focus on the Landau domains with crosstie walls [47].

An in-plane magnetic field is applied to the pattern using an electromagnet with a controlled supply voltage from 0 V to +4.5 V/-3.5V while MFM measurements are taken at different voltages. This procedure is designed to investigate how vortex-antivortex pairs are created and annihilated.

Figure 4.12 shows representative data at the onset of vortex-antivortex pair generation starting from the hard-axis saturated state. The complete series of measurements are in the Appendix 1. In the figure 4.12 (A), the MFM image is taken with an applied magnetic field,  $H= 328$  Oe, which explains why it is relatively featureless except for bright and dark areas along the edges. Since the MFM works by sensing magnetic charges, the image shows that the volume charge density ( $-\text{div}*\mathbf{M}$ ) in the interior is nearly absent but the normal components of the magnetization, the magnetic surface charge density at the opposite side exists.

A CoFeB pattern is expected to be more or less uniformly magnetized along the short axis. As the Zeeman energy, the interaction energy of the magnetization vectors, is reduced, the torque that aligns the moments along the hard axis is reduced, which causes the magnetic charges at the edges to diffuse toward the interior. Figure 4.12 (B) evidently describes the partitioning of the island into three distinct regions that are bounded by strained walls at  $H= 262$  Oe. As the applied magnetic field is

lowered, the middle section that is predominantly aligned with the magnetic field dwindles in size. This phenomenon occurs as when the strained walls are combined and zip upward as the middle section of the magnetic domain collapses from the bottom. By the merger, a  $180^\circ$  Néel wall is generated along the center forming a *vertex*, a core of magnetic vortex, with the strained walls as shown in the figure 4.12 (C). As the magnetic field is reduced to about  $H=89$  Oe, the Néel wall stretches into the bottom and the top part. The motion ceases and the strained walls are transformed into unstrained  $90^\circ$  walls that settle into a  $45^\circ$  angle. Note the smoothness of the  $90^\circ$  wall versus the jaggedness of its strained precursor walls. The boundaries of the top closure structure are created by the  $90^\circ$  walls. In this point, it is more interesting how closure domains are formed to lower the energy. In the top as shown in figure 4.12 (D), the closure domain has a low magnetostatic energy. However there remains still a relatively high-energy state in the rest of the CoFeB pattern. The Néel wall is uniformly magnetized along its entire length and the bottom edge remains highly charged. There is an energy barrier that prevents the simultaneous formation of the top and bottom closure domain structures. This formation happens because the chiralities of the top and bottom vortices are identical, possible only by reversing part of the Néel wall. The transformation into a closure pattern happens at a slightly lower field and is accompanied by the creation of a vortex-antivortex pair that accommodates the reversal of a segment of the Néel wall. This affects the beginning formation of a crosstie wall, which is fortuitously captured in the figure 4.12 (E) at  $H=22$  Oe, undoubtedly expedited by the small fringing field from the probe. As the magnetic field is reduced, more vortex-antivortex pairs appear and the number of

vortex-antivortex pairs is dependent on the balance between the savings in the magneto static energies against the expense of forming cross-ties. However, other experimental data shows the number of cross-ties is diverse between saturation magnetization cycles, suggesting that vortex-antivortex generation can be affected profoundly by local pinning effects or slight variations in the switching fields.

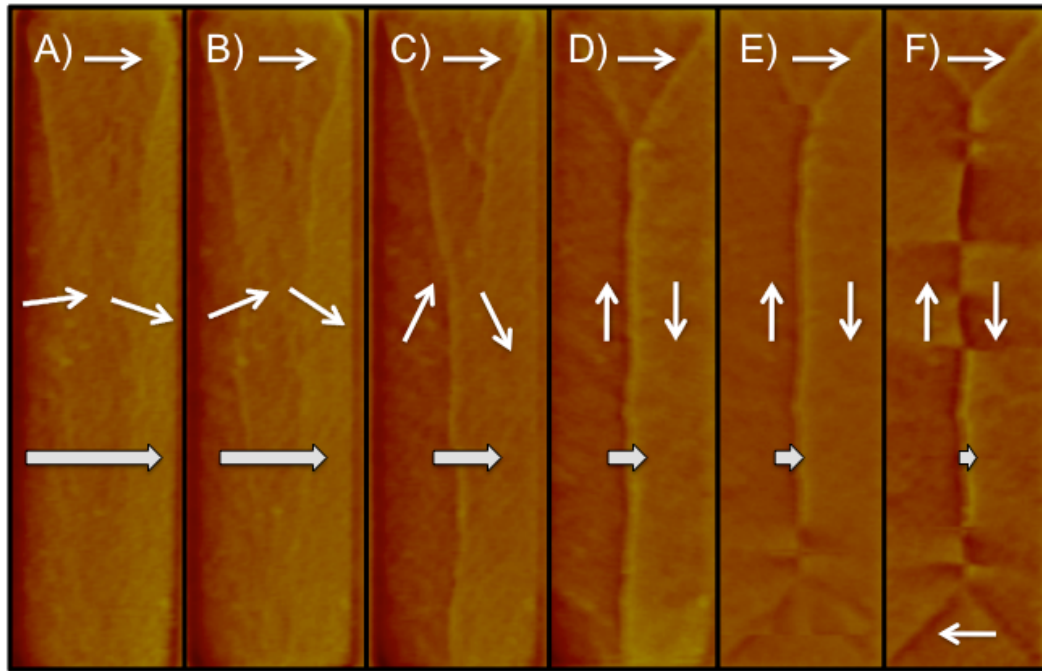


Figure 4.12 Formation of vortices from a saturated state. MFM images were taken in the presence of field applied along the short axis, sequentially decreasing from A) 328 Oe, B) 262 Oe, C) 185 Oe, D) 89 Oe, E) 22 Oe and F) 11 Oe. The thin arrows indicate the orientation of the magnetization in the domains, and bold arrows indicate the direction of applied field and relative strength.

In figure 4.13, the annihilation process is observed, as the field is increased from zero to  $H=185$  Oe. These MFM images consist of a representative subset of a large number of images taken every  $\sim 10$  Oe. At the remanent state, there exist 10 vortex-antivortex pairs and each one is designated by unprimed and primed numbers. It is significant to note that the first and last “vortices” (which are the vertex of the closure pattern) are created in different environments than those in the interior.

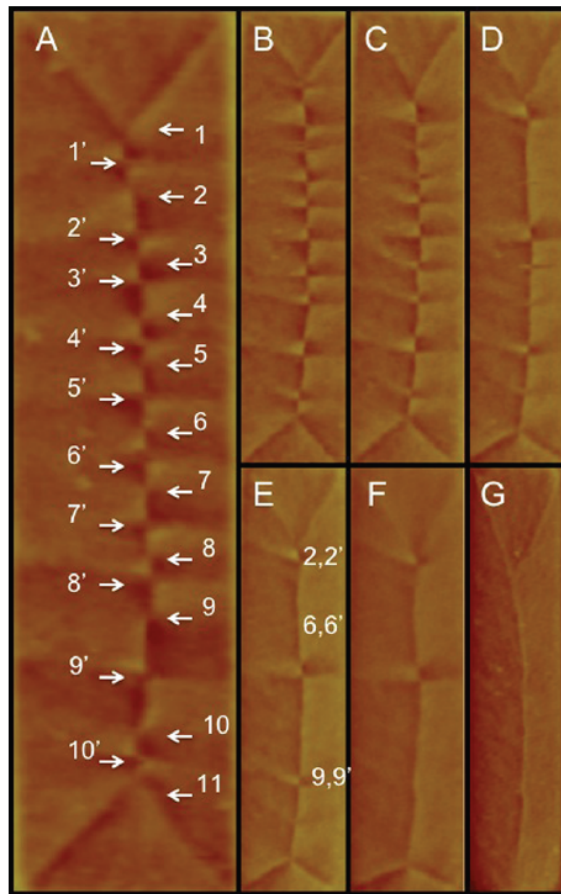


Figure 4.13 Annihilation of vortices from remanent to saturation. This is a subset obtained from many images at various field increments. Images shown at A)  $H=0$ , B) 30 Oe, C) 59 Oe, D) 89 Oe, E) 118 Oe, F) 147 Oe, G) 185 Oe. On A), vortices and vortices are labeled with primed and unprimed numbers.

In figure 4.14, the vortex-antivortex locations versus externally applied magnetic fields elicited from the MFM images are summarized for facilitation of the analysis. In this process, several characteristics are obtained. First, the mobility of vortices is higher relative to the antivortices. This observation has been previously discussed by others investigating the stiffening of the antivortices due to the charges created from the transverse Néel wall. Second, with one exception, all the vortices move in the same direction, downwards. This discovery is possible since the vortex motion occurs as a result of the expansion of the sections of the  $180^\circ$  Néel wall parallel to the direction of the applied magnetic field. All segments can only be extended in one direction because the other end is anchored by a fixed antivortex. Third, in a range of the applied magnetic field between  $H= 38$  Oe to  $78$  Oe, most of the displacement occurs. Below  $H= 38$  Oe, vortex motion does not happen; a threshold field is necessary for origination of the movements. Several pairs annihilate within this range (3,3', 4,4' and 5,5') and all other vortices move by relatively large distances. As shown in figure 4.14, it is suggested that the vortex displacement is proportional to the initial pair spacing. So the vortices appear to move fairly easily until they reach a specific distance from their antivortex partner, beyond which they need higher field increments to draw them closer. Apparently, the magnetic charge density becomes greater between the pairs as the distance between vortex-antivortex decreases. As a result, the demagnetization fields increase, but the local susceptibility is reduced. The motion of the pairs in the vicinity of the top closure domain appears to be somewhat different from those farther into the interior. The top vortex (1) moves downward as the closure domain enlarges. At  $H= 44$  Oe, it instantaneously appears that antivortex

1' and vortex 2 merge and continue to persist at higher fields until it combines with the highly stable antivortex 2'.

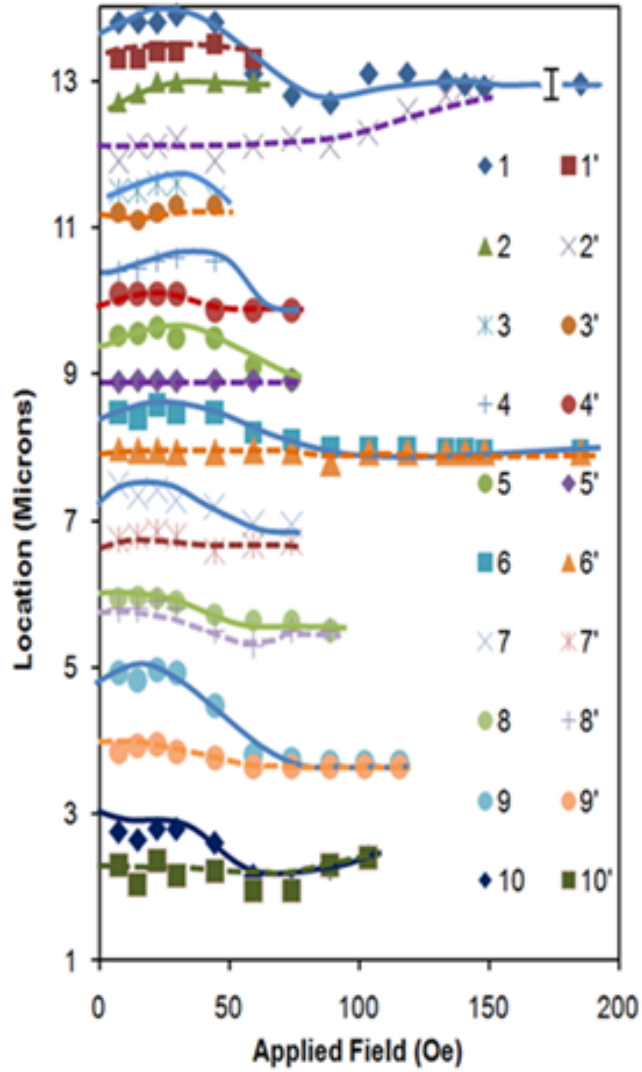


Figure 4.14 Plot of the location of all vortices and antivortices. The uncertainty for determining the core position is  $\pm 0.2 \mu\text{m}$ , shown in the error bar.

Finally, the annihilation process of vortex-antivortex pairs is discussed. This phenomenon is influenced by many factors and an accurate explanation could not be conclusively established in one experiment. For example, the effect of the variations of the local coercivity, which is a necessary field for changing the direction of magnetization, and other defects cannot totally be decided. However, some qualitative insights can be taken from the data. Apparently, there is a distribution of annihilation field ( $H_x$ ) starting from  $H= 44$  Oe to 185 Oe. As shown in figure 4.14, the most persistent pair is (6,6'), followed by (2,2') and (9,9'). These structures are nearly equidistant from each other, which suggests that the annihilation process is determined by long-range interaction as opposed to the nanoscale structure. This is a general phenomenon observed consistently in almost all samples. Indeed, the minimization of the magnetostatic energy of the wall appears to be the main determinant of annihilation. Similarly spaced Néel walls between vortex-antivortex pairs ensure the equal distribution of the magnetostatic energy across the entire length of the cross-tie wall.

This leads us to the role of the core polarity. Despite its relatively small size, it is possible to discern the orientation from the contrasts of high-resolution MFM images[48]. However, in this specific sample, it is difficult to conclusively establish the core polarity in all cases because of the limited number of pixels per core consistent with the large field of view. Nevertheless the relative polarity for each pair can be discerned from the differences in contrasts between the vortex and antivortex cores. Based on careful inspection, it cannot be inferred that the core polarity plays a role in the annihilation process. Our results are different from the findings of others

who discovered that antiparallel vortex-antivortex cores are more difficult to annihilate. The main difference is the size and shape of the islands. In their case, the islands only are hundreds of nanometers large, and can support a single vortex core. Thus, they were able to isolate the core effects. However, our results indicate that the role of polarity can be masked in a series of many vortex-antivortex pairs.

## **Chapter 5. Future work**

### **5.1 Control of core direction of vortex-antivortex with applying out-of plane magnetic field**

As shown in chapter 4.4, magnetic cross-tie domains with vortices and antivortices were observed in the CoFeB islands of 55 nm thickness. Creation and annihilation of vortex-antivortex pairs are shown by MFM images, when an in-plane magnetic field is applied to the patterns. Based on this result, control of core polarity between vortex and antivortex pairs will be possible if an out-of-plane external magnetic field with is applied[49]. Controlling core direction of vortex-antivortex pairs at a certain magnetic field will be employed by vortex-random access memory (VRAM)-antivortex-random access memory (AVRAM)[3].

Figure 5.1 shows experimentally obtained MFM images of the cross-tie wall and expected schematic illustrations of the magnetization confined in a rectangular pattern with the size  $9\ \mu\text{m} \times 3\ \mu\text{m}$ . The blue and red spots at the cores of the vortices correspond to the direction of the perpendicular magnetization component, since the direction at all cores aligns to that of the applied field for the image in figure 5.1.

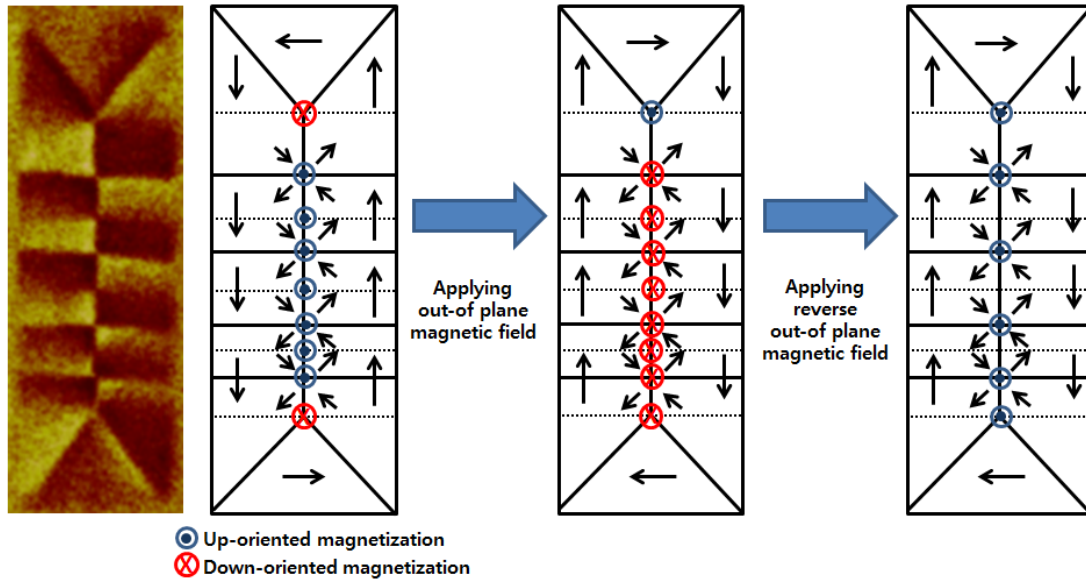


Figure 5.1 Obtained MFM image and expected schematic illustrations of realized magnetization distribution.

## 5.2 Investigation of CoFeB patterns on MgO[100] substrate

Recently, the importance of CoFeB/MgO/CoFeB structures has been recognized and applied to the Spin Transfer Torque (STT) device as well, for obtaining a high Tunneling Magneto Resistance (TMR) effect. In the structure of a magnetic tunnel junction (MTJ) device, CoFeB electrodes might be crystallized locally near the interfaces after annealing at a temperature of around 400 °C for 1 hour, because the MgO[001] layer could act as a template to crystallize a CoFeB layer[33][34][35].

Instead of Si/SiO<sub>2</sub> substrate, magnetic domains in CoFeB islands on an MgO[100] substrate will be investigated to study the crystallization of the CoFeB layer. In this experiment, there are two possible methods for the formation of CoFeB patterns.

With a cleaned MgO substrate, first a CoFeB film is uniformly deposited by sputtering without any patterning. The e-beam writing process is performed on the

CoFeB film for formation of micron/nano-sized patterns and ER patterns are formed by developing with the developer of MIBK:IPA(1:3). Then, CoFeB is patterned by a dry etching such as an ion milling process, where the ER acts as a hard mask during etching process[51]. Next, ER patterns are removed by Acetone and favorable CoFeB patterns are identified. In figure 5.2, the fabrication process of CoFeB pattern using an etching technique is shown.

*# Fabrication Process of CoFeB Pattern on MgO Substrate(Etching)*

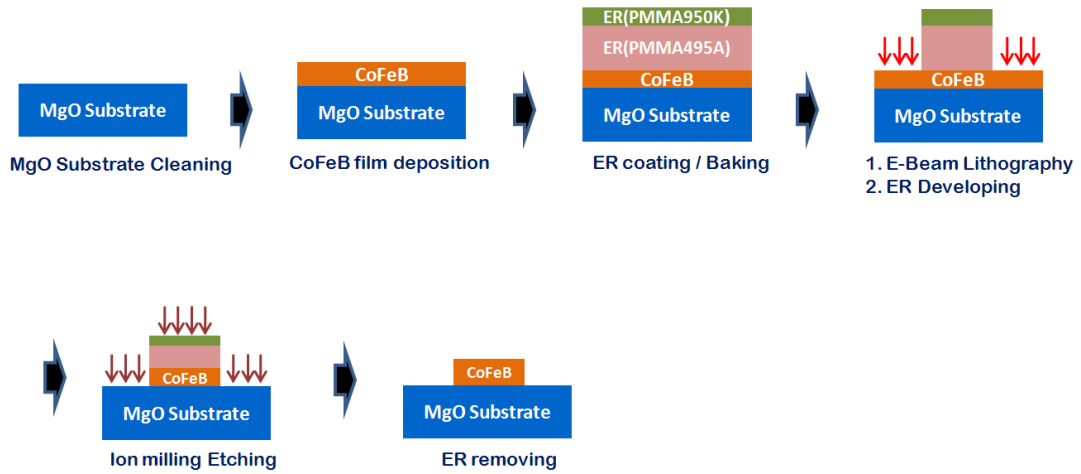


Figure 5.2 Fabrication process of CoFeB pattern using etching technique.

Another way is to create selective patterns before deposition of CoFeB as follows. First, two kinds of e-beam resist (ERs) are deposited respectively, to create an undercut structure for the e-beam writing process. Because MgO substrate is dielectric material, electrons cannot penetrate the MgO layer directly without a thin metal layer like Al. For solving this problem, Al film is additionally deposited with a 10~20 nm thickness on the ER layers and the e-beam writing process is performed for

the formation of micron/nano-sized patterns. CoFeB is deposited by sputtering for formation of domain structure, and the devices were annealed at the constant temperature of 400 °C for 1hr, after the lift-off process.

Before the developing process, the Al layer is removed with an Al etchant like OPD 4262 and ER patterns are developed with MIBK:IPA(1:3). In figure 5.3, the total lift-off process is shown.

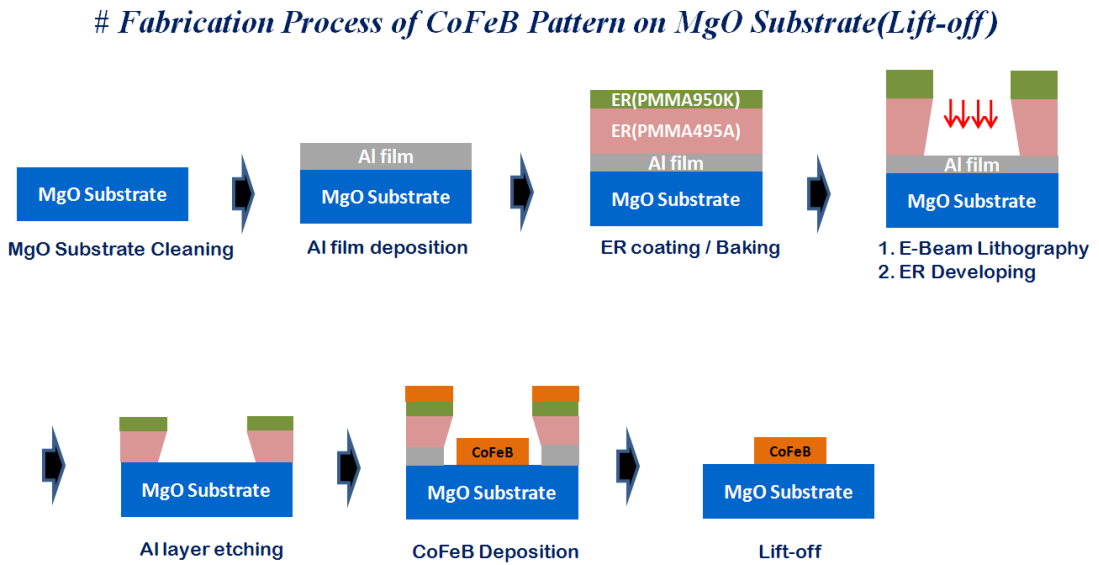


Figure 5.3 Fabrication process of CoFeB pattern using lift-off technique.

### **5.3 Ferromagnetic resonance (FMR) experiment using cross-tie walls of CoFeB islands[7][8]**

Recently, magnetization dynamics of CoFeB patterns like vortex-antivortex creation and annihilation, domain wall motion, and ferromagnetic resonance (FMR) have been extensively gaining much attention because of the possibility of the application to storage and spintronics applications[52][53][54][55]. However, broadband electrical detection of magnetic phenomena at the micro/nanoscale is very different. Measurement sensitivity is strongly affected by on the physical process of detection and in many cases it leads to a small signal-to-noise ratio (SNR) for individual micro/nanoscale devices. A possible approach is the use of a ferromagnet with cross-tie domain walls[56][57][58][59]. However, magnetostatic and dynamic interactions of the ferromagnet device, controlled by size and thickness of the device, influence the response and therefore the response may not express the property of an individual pattern.

In this research, all-electrical measurements to characterize the field dependence of static magnetization states as well as magnetization dynamics within periodical magnetic patterns are used and differential resistance  $dV/dI$ , spin rectification effect, inductive techniques, and rf/microwave transmission measurements will be included[60][61][62][63][64].

First, a CoFeB ferromagnet is formed, cross-tie walls with vortex-antivortex pairs are observed within micron-nanoscale structures, and contact pads fabricated by Ti/Au are added for electrical contacts, to investigate FMR through measurement. In this experiment, differential resistance ( $dV/dI$ ) measurements give information on the

static magnetization states as a function of applied. The  $dV/dI$  technique utilizes the anisotropic magneto-resistance (AMR) effect to detect changes in magnetization. Magnetization dynamics in non-saturated elements are characterized by  $dV/dI$  measurements combined with a radio frequency (RF) driving field. For saturated elements, the rectification effect is also utilized. Figure 5.4 shows the fabrication process of a FMR device from sample cleaning to ferromagnet formation to contact pad formation. Considering several measurement methods, two types of photo-masks are designed and shown in the following appendix. In Figure 5.5 and 5.6, microscopic images after formation of the CoFeB ferromagnet and the Ti/Au contact pads are shown.

# Fabrication Process of FMR device

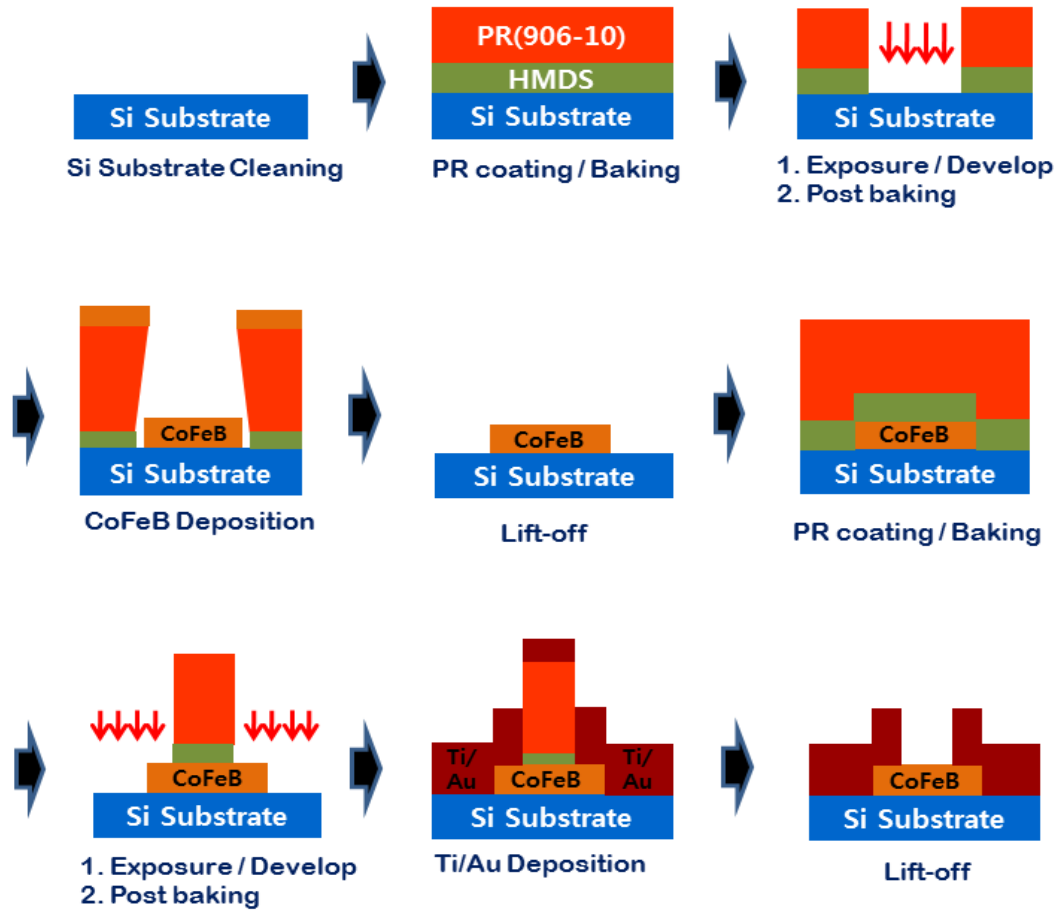
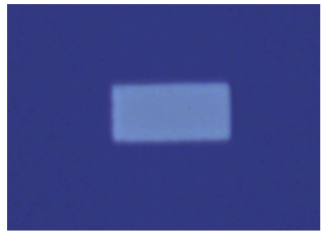
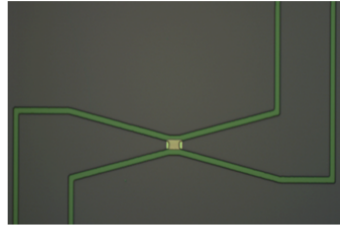


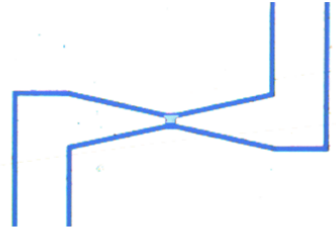
Figure 5.4 Fabrication process of FMR device.



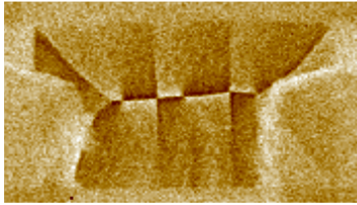
(a) After ferromagnet formation



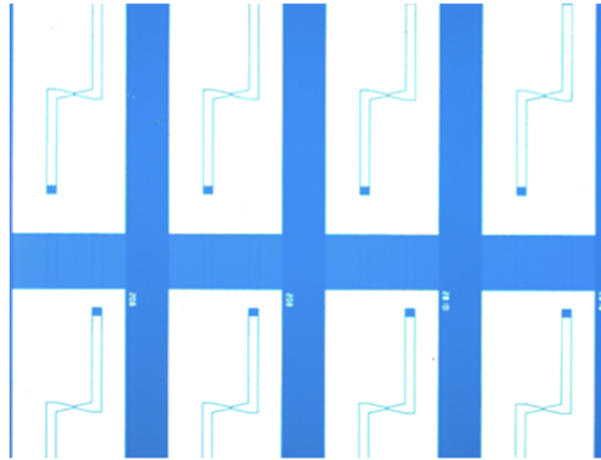
(b) After contact pads patterning



(c) After contact pads formation

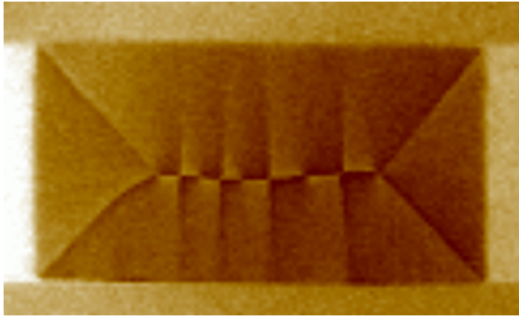


(d) After MFM measurement

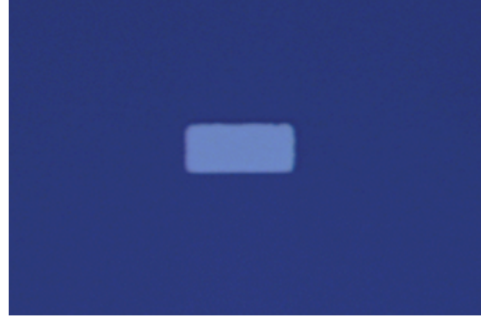


(e) After MFM measurement of contact pads(Ti/Au)

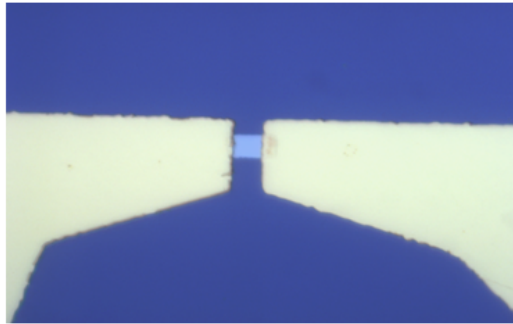
Figure 5.5 microscopic images after formation of CoFeB ferromagnet and Ti/Au contact pads.



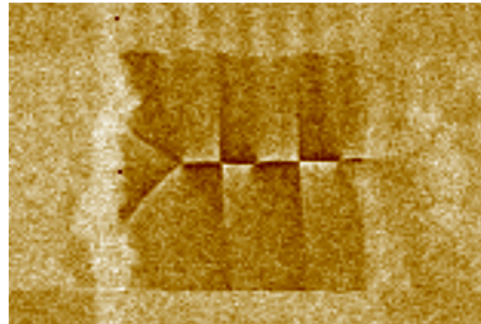
**(a) After MFM measurement of ferromagnet(16 $\mu$ m x 8 $\mu$ m)**



**(b) After ferromagnet formation**



**(c) After contact pads formation**



**(d) After MFM measurement of Contact pads(Ti/Au)**

Figure 5.5 microscopic images after formation of CoFeB ferromagnet and Ti/Au contact pads.

## Chapter 6. Conclusion

The main objective of this thesis is to investigate how vortex-antivortex pairs are created and annihilated according to the externally applied in-plane magnetic fields in CoFeB islands on Si substrate.

First, this experiment shows several magnetic domain configurations of CoFeB islands with different sizes, film thicknesses, and aspect ratios between length and width. The domain configuration depends on intrinsic material properties, dimensions of the pattern, and the method of film growth. To make some types of magnetic domain in a specific ferromagnetic material, the aspect ratio, thickness and crystalline direction are controlled.

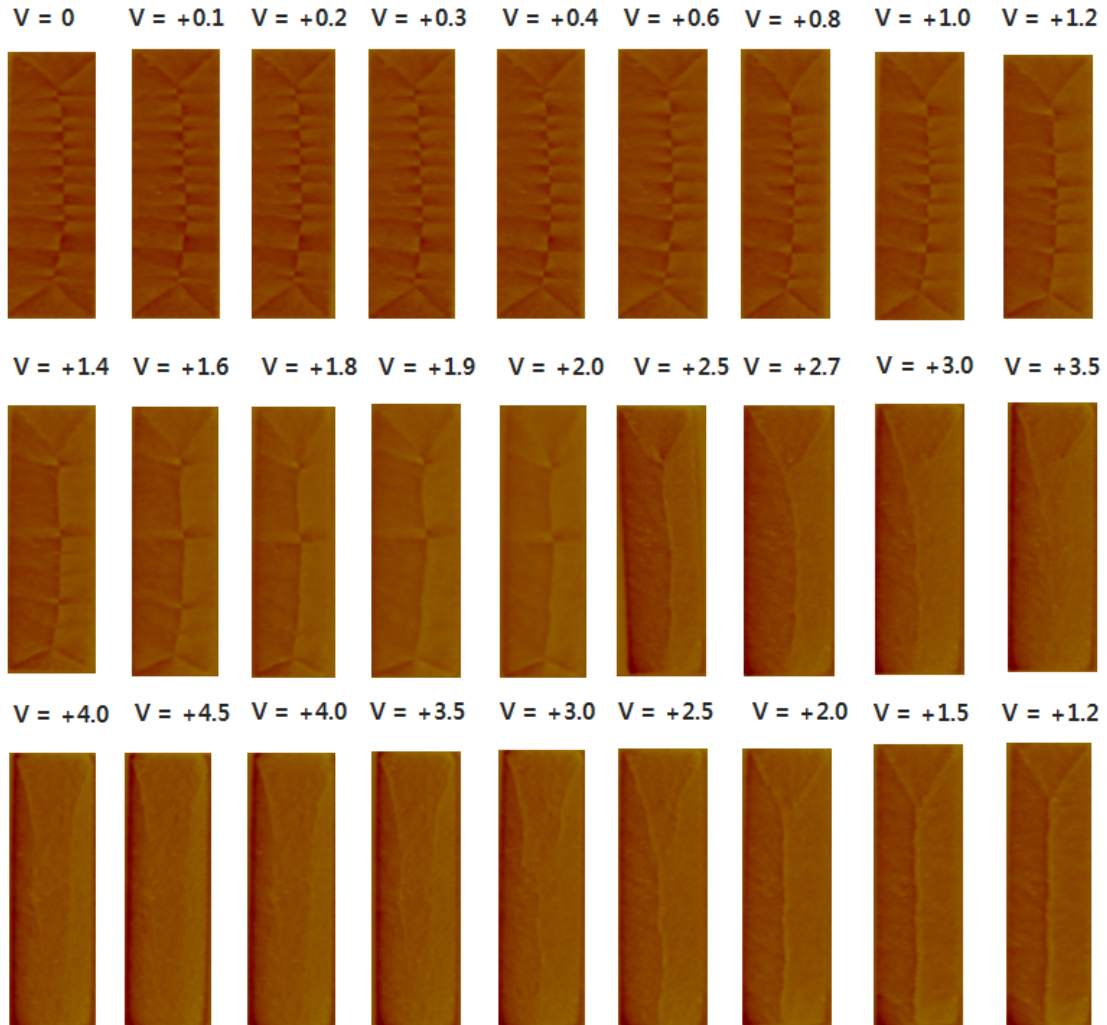
To investigate the creation and annihilation of vortex-antivortex pairs, a pattern with the size of  $16\ \mu\text{m} \times 4\ \mu\text{m}$  and a thickness of 50nm, where cross-tie domain walls with magnetic vortex-antivortex pairs are observed, is chosen from several patterns and measured by MFM while applying in-plane magnetic field. As a result, the quasistatic process of creation and annihilation of a linear array of vortex-antivortex pairs exhibit rich and interesting characteristics that are governed by the macroscopic minimization of energy.

Future directions in further developing this experiment are to investigate the controlling of the core polarity of vortex-antivortex pairs by applying out-of plane magnetic fields and use a new substrate like MgO[100], instead of a Si substrate. In addition, ferromagnetic resonance (FMR) measurements using CoFeB ferromagnets are expected to show how the cross-tie walls with magnetic vortex-antivortex pairs

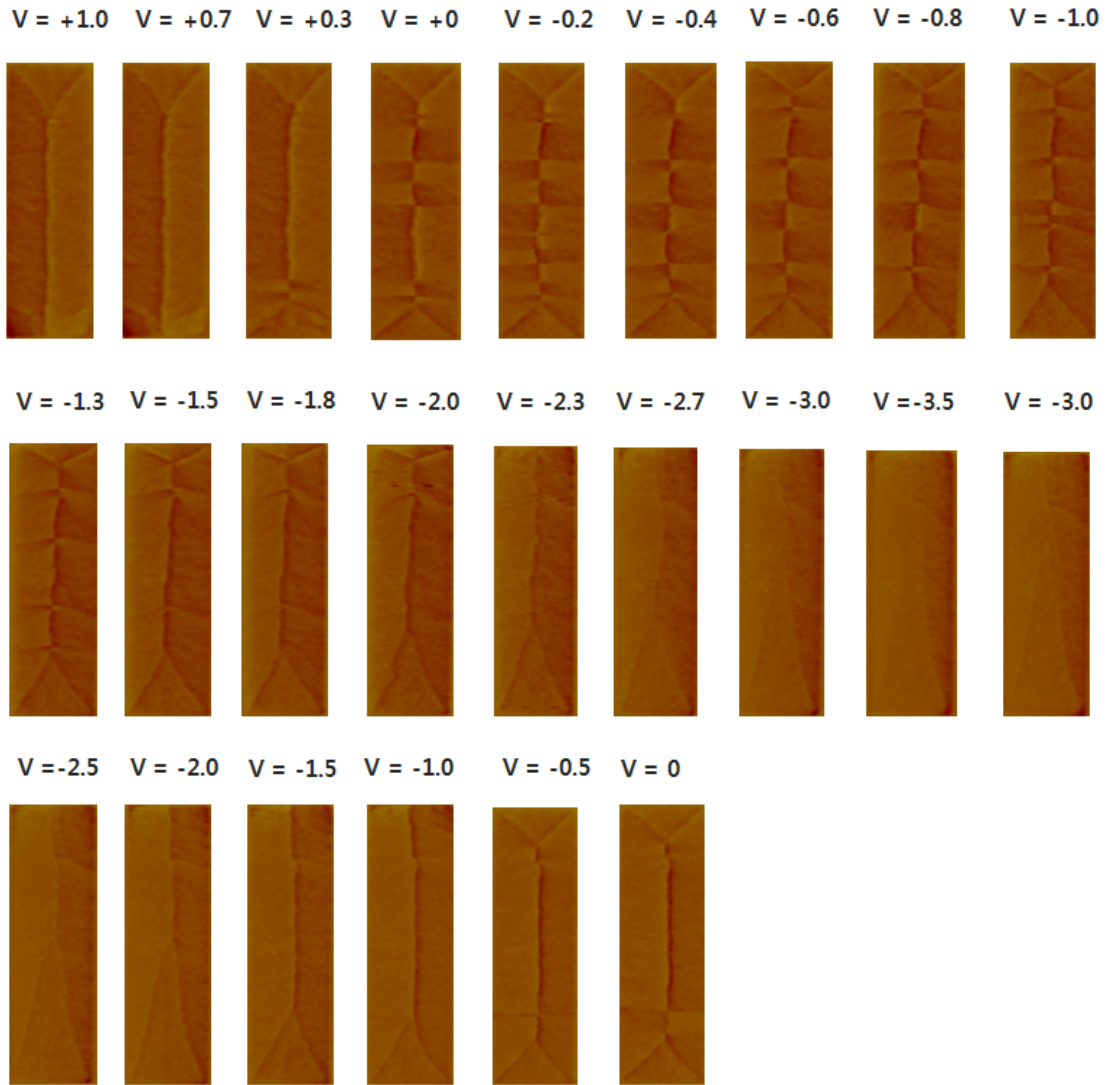
change. We will implement this investigation using FMR measurements and this part is the topic of a Ph.D dissertation.

## Appendices

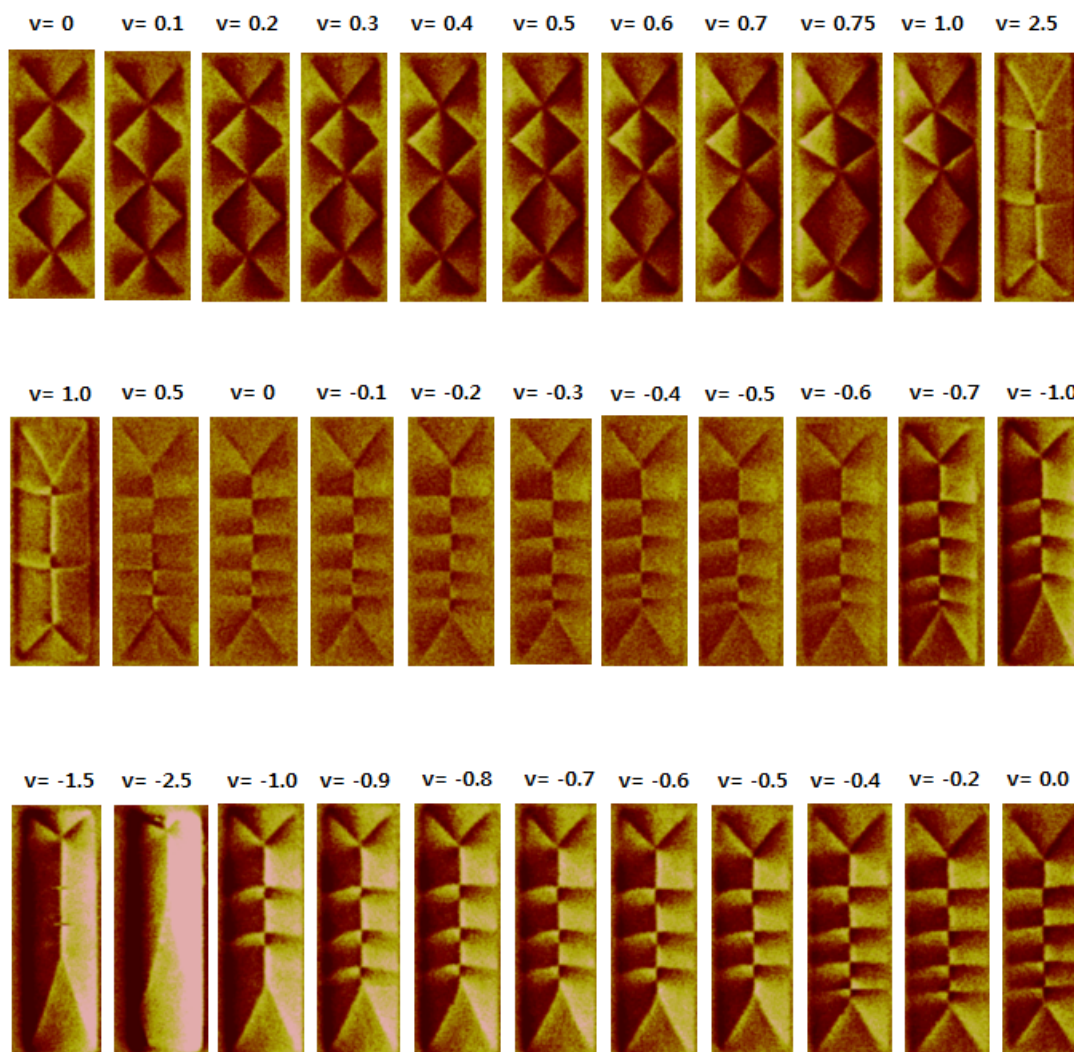
A.1 MFM images of  $16\mu\text{m} \times 4\mu\text{m}$  CoFeB islands over a complete magnetization cycle.



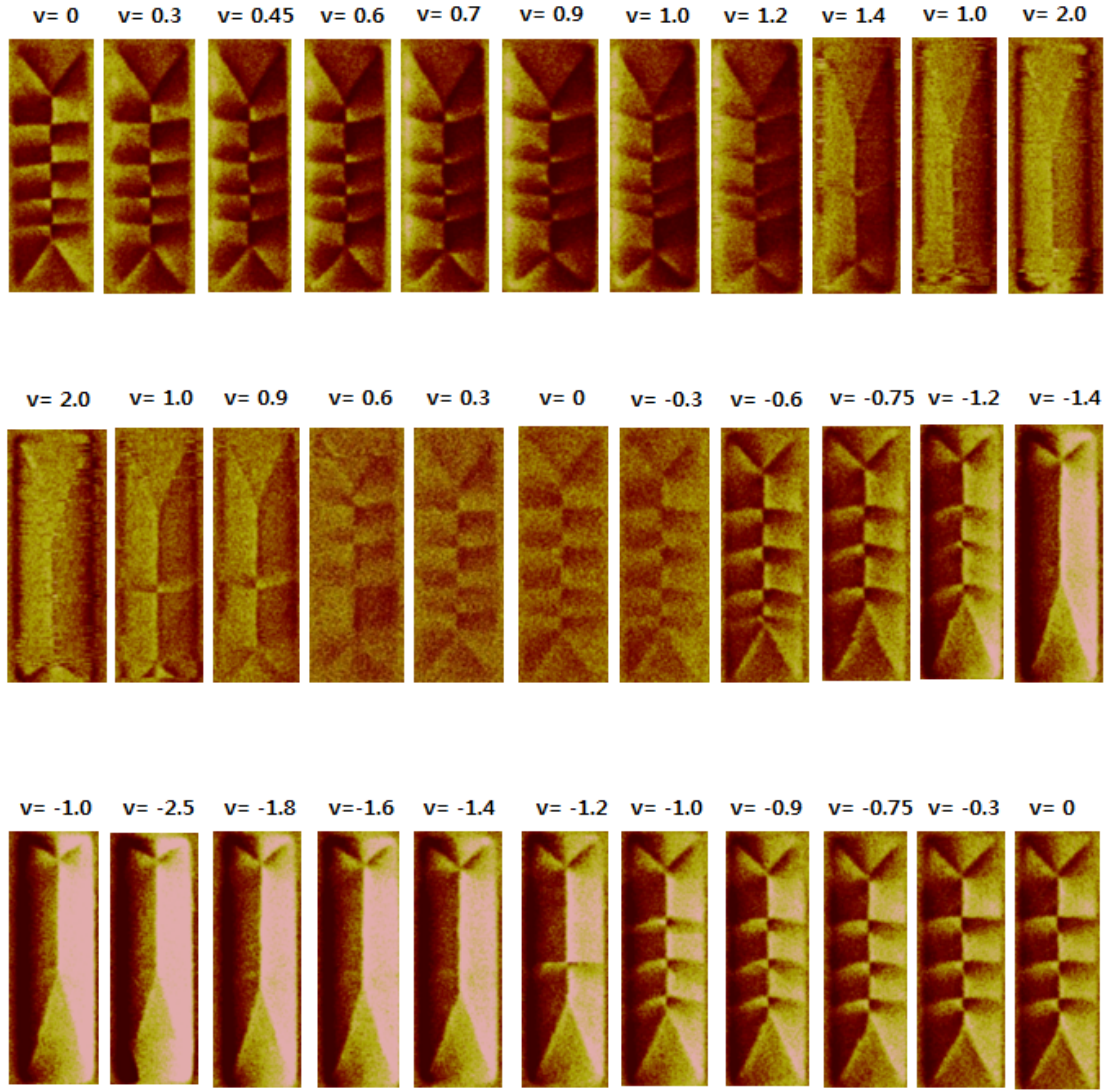
A.2 MFM images of  $16\mu\text{m} \times 4\mu\text{m}$  CoFeB islands over a complete magnetization cycle.



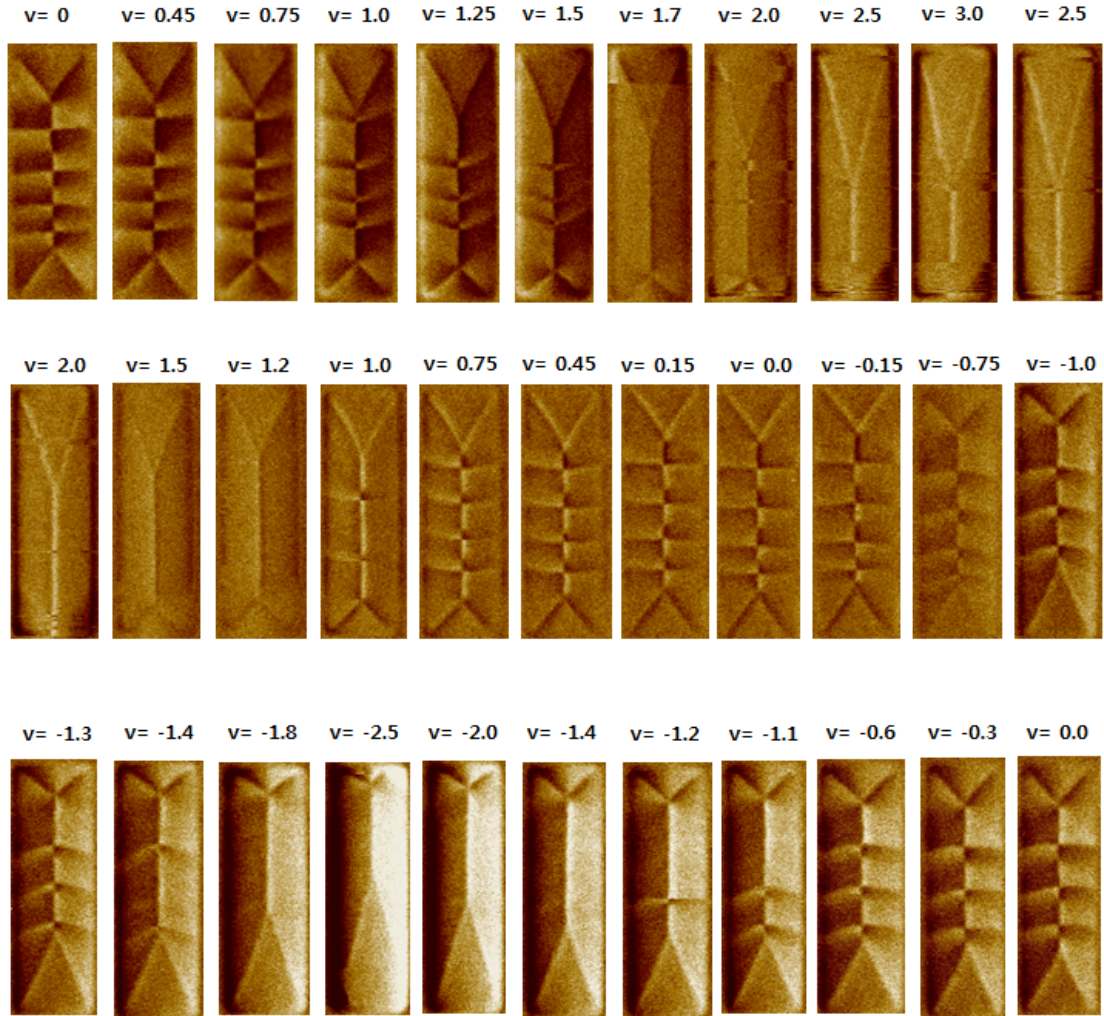
A.3 MFM images of  $9\mu\text{m} \times 3\mu\text{m}$  CoFeB islands with various applied magnetic fields



A.4 MFM images of  $9\mu\text{m} \times 3\mu\text{m}$  CoFeB islands with various applied magnetic fields



A.5 MFM images of  $9\mu\text{m} \times 3\mu\text{m}$  CoFeB islands with various applied magnetic fields



#### A.6 Fabrication procedure of CoFeB patterns on the Si substrate

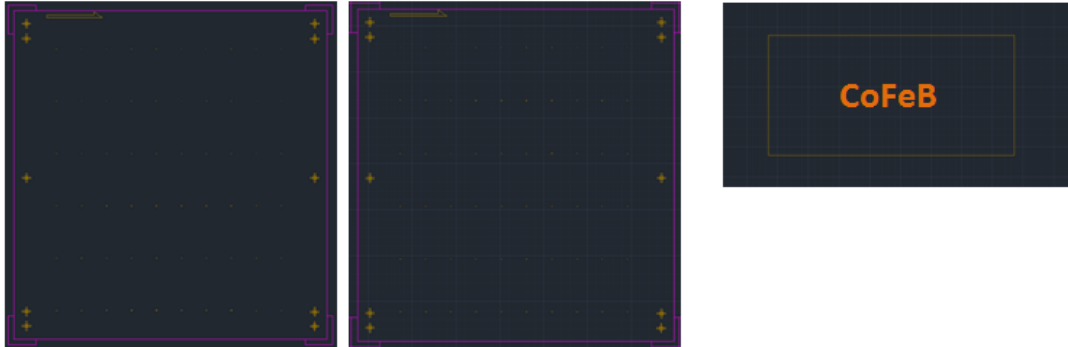
<b>Step</b>	<b>Description</b>
Spin coating	Resist : PMMA 495A, Speed : 5,000 RPM, Time : 1 min
Bake resist	Bake type : Hot plate, Temperature : 170°C, Time : 15 mins
Spin coating	Resist : PMMA 950K, Speed : 5,000 RPM, Time : 1 min
Bake resist	Bake type : Hot plate, Temperature : 170°C, Time : 15 mins
Exposure	E-beam current : 15 ~ 18 pA, Does paramenter : 250 $\mu\text{C}/\text{cm}^2$
Develop	Developer : IPA:MIBK(1:3),Time : 1 min, Rinse : IPA
Plasma etching	Gas : O <sub>2</sub> , Power : 100W, Time : 15 secs
Sputtering (CoFeB)	Sputtering type : DC sputtering, Base pressure : 5.5 mTorr Deposition rate : 6 nm / min
Lift-off	Solvent : Acetone, Time : overnight

### A.7 Fabrication procedure of an FMR device

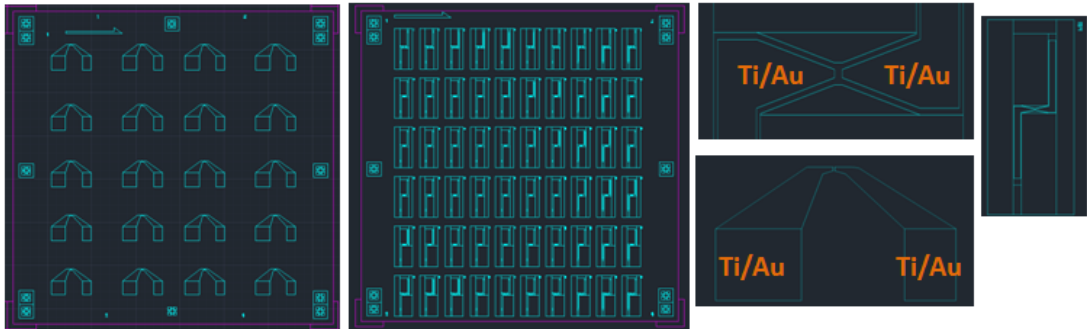
<b>Step</b>	<b>Description</b>
Spin coating	Photo resist : 906-10, Speed : 5,000 RPM, Time : 1 min
Bake resist	Bake type : Hot plate, Temperature : 95°C, Time : 1 min
Exposure	Power : 12 mW, Time : 3.2 secs
Post bake	Bake type : Hot plate, Temperature : 120°C, Time : 1 min
Develop	Developer : OPD 4262, Time : 1 min, Rinse : DI water
Plasma etching	Gas : O <sub>2</sub> , Power : 100W, Time : 15 secs
Sputtering (CoFeB)	Sputtering type : DC sputtering, Power : 73 Watt Base pressure : 5.5 mTorr, Deposition rate : 6 nm / min
Lift-off	Solvent : Acetone, Time : overnight
Spin coating	Photo resist : 906-10, Speed : 5,000 RPM, Time : 1 min
Bake resist	Bake type : Hot plate, Temperature : 170°C, Time : 15 mins
Exposure	Power : 12 mW, Time : 3.2 secs
Post bake	Bake type : Hot plate, Temperature : 120°C, Time : 1 min
Develop	Developer : OPD 4262, Time : 1 min, Rinse : DI water
Plasma etching	Gas : O <sub>2</sub> , Power : 100W, Time : 15 secs
Evaporation (Ti/Au)	Evaporation type : E-beam, Base pressure : $-2 \times 10^{-6}$ Torr, Deposition rate : 6 Å / sec, Thickness : 10 nm(Ti) /100nm(Au)
Lift-off	Solvent : Acetone, Time : overnight

## A.8 Photolitho-mask design of FMR device

### A. Photo Mask Design of FM(Ferromagnet)



### B. Photo design of Contact pads



## References

- [1] J. M. Daughton, “Magnetic tunneling applied to memory”, *J.Appl, Phys.*, Vol. 81, 1997.
- [2] M. Johnson, “Magnetoelectronic last and last,” *IEEE Spectrum*, Vol. 37, 2000.
- [3] B. Pigeau, “A frequency-controlled magnetic vortex memory”, *Applied Physics Letters*, vol. **96**, 132506, 2010.
- [4] H. Koo, T.V. Luu, R.D.Gomez, and V.V. Metlushko “Slow magnetization dynamics of small permalloy islands,” *J.Appl, Phys.*, Vol. 87, 2000.
- [5] R. D. Gomez, J. S. Ma, A. Arkilic, S. H. Chung, and C. Krafft, “Vortex-antivortex creation and annihilation on CoFeB crosstie patterns”, *J.Appl, Phys.*, Vol. 109, 2011.
- [6] K. Shigeto, T. Okuno, K. Mibu, and T. Shinjo, “Magnetic force microscopy observation of antivortex core with perpendicular magnetization in patterned thin film of permalloy”, *Applied Physics Letters.*, Vol. 80, 2002.
- [7] Sang-Hyun Lim<sup>1</sup>, T. Mitch Wallis, Atif Imtiaz, Dazhen Gu, Pavol Krivosik, and Pavel Kabos “Influence of Periodic Patterning on the Magnetization Response of Micromagnetic Structures”, *IEEE MAGNETICS LETTERS*, Vol. 2, 2011.
- [8] Sang-Hyun Lim, T. M. Wallis, Atif Imtiaz, Dazhen Gu, Pavol Krivosik, and Pavel Kabos, “Comparison of electrical techniques for magnetization dynamics measurements in micro/nanoscale structures”, *J. App. Phys.*, vol. 109, 2011.
- [9] T.V Luu, Domain wall motion in small elements of permalloy as observed using magnetic force microscopy, *Master’s thesis*, University of Maryland, ch. 2,4, 1999.
- [10] [cwscholz.net/projects/da/node7.html](http://cwscholz.net/projects/da/node7.html)

- [11] [Gitam.edu/eresource/Engg\\_Phys/semester\\_2/magnetic/domain.htm](http://Gitam.edu/eresource/Engg_Phys/semester_2/magnetic/domain.htm)
- [12] F. Keffer, *Handbuch der Physik*, 18, pt. 2, New York: *Springer-Verlag*, 1966.
- [13] R. M. White, *Introduction to magnetic recording*, New York : *IEEE press*, ch. 2, 1985.
- [14] M.Prutton, *Thin Ferromagnetic Films*, Butterworth & Co.Ltd, Washington DC, 1964.
- [15] Jeffrey McCord' "Domain wall asymmetries in Ni<sub>81</sub>Fe<sub>19</sub>/NiO: proof of variable anisotropies in exchange bias systems", *New Journal of Physics*, Vol 11, 2009.
- [16] Middelhoeck, " Domain walls in thin Ni-Fe films", *J. Appl. Phys.* Vol. 34, 1963.
- [17] DeSimone A, Kohn R, Müller S and Otto F, "Recent analytical developments in micromagnetics", *The Science of Hysteresis*, vol. 2, 2005.
- [18] Schäffel F 2004 Observation of domain walls in amorphous CoZrTa and FeCoBSi thin films *Diploma Thesis*, Technical University of Dresden.
- [19] Hubert A and Schäfer R 2008 *Magnetic Domains* 3rd edn (Berlin: Springer).
- [20] T.Shinjo etal., *Science*, 289,930, 2000.
- [21] [lambda.pha.jhu.edu/.../interests/nanoring.html](http://lambda.pha.jhu.edu/.../interests/nanoring.html).
- [22] A. Wachowiak etal., *Science* 298,577, 2002.
- [23] A. S. Arrott and T. L. Templeton, *Physica (Amsterdam)* 233B, 259, 1997.
- [24] T. Shinjo, T. Okuno, R. Hassdorf, K. Shigeto, and T. Ono. "Magnetic vortex core observation in circular dots of permalloy." *Science*, 289, 930, 2000.
- [25] A. Wachowiak, J. Wiebe, M. Bode, O. Pietzsch, M. Morgenstern, and R. Wiesendanger, *Science* **298**, 577, 2002.
- [26] J. Miltat and A. Thiaville, *Science* **290**, 466, 2000.

- [27] S. B. Choe, Y. Acremann, A. Scholl, A. Bauer, A. Doran, J. Stohr, and H. A. Padmore, *Science* **304**, 420, 2004.
- [28] J. P. Park, P. Eames, D. M. Engebretson, J. Berezovsky, and P. A. Crowell, *Phys. Rev. B* **67**, 020403(R), 2003.
- [29] A. Puzic, B. Van Waeyenberge, K.W. Chou, P. Fischer, H. Stoll, G. Schuetz, T. Tylizszak, K. Rott, H. Brueckl, G. Reiss, I. Neudecker, T. Haug, M. Buess, and C. H. Back, *J. Appl. Phys.*, vol. **97**, 10E704, 2005.
- [30] Riccardo Hertel, Exchange Explosions: Magnetization Dynamics during Vortex-Antivortex Annihilation, *PHYSICAL REVIEW LETTERS*, 97, 177202, 2006.
- [31] E. E. Huber, Jr., D.O. Smith, and J. B. Goodenough, *J. Appl. Phys.*, Vol. **29**, 1958.
- [32] R. D. Gomez, T. Luu, A. Pak, K. Kirk, and J. Chapman, *J. Appl. Phys.*, Vol. **85**, 1999.
- [33] D. D. Djayaprawira, "230% room temperature magnetoresistance in CoFeB /MgO/CoFeB magnetic tunnel junctions," *INTERMAG ASIA 2005: Digests of the IEEE International Magnetism Conference*, 2005.
- [34] J. Hayakawa, "Effect of high annealing temperature on giant tunnel magnetoresistance ratio of CoFeB/MgO/CoFeB magnetic tunnel junctions," *Applied Physics Letters*, vol. 89, 2006.
- [35] [Arzuffisrl.it/eng/sputtering.htm](http://Arzuffisrl.it/eng/sputtering.htm)
- [36] [Eetafilm.com.tw/PVD\\_Sputtering\\_Deposition.html](http://Eetafilm.com.tw/PVD_Sputtering_Deposition.html)

- [37] D. Rugar, H. J. Mamin, P. Guethner, S. E. Lambert, J. E. Stern, I. McFadyen, and T. Yogui, "Magnetic force microscopy : General principles and application to longitudinal recording media," *J. Appl. Phys.*, vol. 68, 1990.
- [38] H. J. Mamin, D.Rugar, J. E. Sterns, R.E Fontana Jr., and P. Kasiraj, "Magnetic force microscopy of thin Permalloy films," *Applied Physics Letters.*, vol. 55, 1989.
- [39] H. J. Mamin, D.Rugar, J. E. Fontana, J. E. Stern, B. D. Terris and S. E. Lambert, "Force microscopy of magnetization patterns in longitudinal recording media," *Applied Physics Letters.*, vol. 53, 1988.
- [40] Y. Martin and H. K. Wickramasinghe, "Magnetic imaging by force microscopy with 1,000 Å resolution," *Applied Physics Letters.*, vol. 50, 1987.
- [41] P. C. D. Hobbs, D. W. Abraham, and H. K. Wickramasinghe, "Magnetic force microscopy with 25 nm resolution," *Applied Physics Letters.*, vol. 55, 1989.
- [42] R. D. Gomez, "Recent advances in magnetic force microscopy : Quantification and in-situ field measurements" in *Experiment Methods in the Physical Sciences*, vol. 36, M.de Graef and Y. Zhu, editors, Academic Press, 2001.
- [43] R. D. Gomez, E. R. Burke, and , I. D. MayerGOYZ, "Magnetic imaging in the presence of external fields: Technique and application," *J.Appl, Phys.*, Vol. 79, 1996.
- [44] J. F. Smyth, S.Schultz, D.R. Fredkin, D.P. Kern, S. A. Rishton, H.Schmidt, and M.Cali, "Hysteresis in lithographic arrays of permalloy partiles : Experiment and theory," *J. Appl, Phys*, 69 5262(1991).
- [45] J. G. Zhu, Y.Zheng, and X.Lin,"Micromagnetics of small size patterned exchange biased Permalloy film elements," *J.Appl. Phys.*, vol. 81, 1997.

- [46] T. Schrefl, J. Fidler, K.J. Kirk, and J. N. Chapman, "Domain structures and switching mechanisms in patterned magnetic elements," *J. Mag. Magn.Mat.* vol. 175, 1997.
- [47] R. D. Gomez, J. S. Ma, A. Arkilic, S. H. Chung, and C. Krafft, "Vortex-antivortex creation and annihilation on CoFeB crossbar patterns", *J.Appl. Phys.*, vol. 109, 2011.
- [48] K. Shigeto, T. Okuno, K. Mibu, T. Shinjo, and T. Ono, *Applied Physics Letters.*, vol. 80, 4190 2002.
- [49] M. F. Lai, Z.-H. Wei, J. C. Wu, W. Z. Shieh, C. R. Chang, and J. Guo, *J. Appl. Phys.* Vol. 101, 2007.
- [50] K. Shigeto, T. Okuno, K. Mibu, and T. Shinjo, "Magnetic force microscopy observation of antivortex core with perpendicular magnetization in patterned thin film of permalloy" *Applied Physics Letters.*, vol. 80, 2002.
- [51] Danielle S. Hines, Kurt E. Williams, Mark S. Campo, "Reactive Ion Beam Etching of InP", *Application note 02681*, Veeco Instruments Inc. Plainview, NY.
- [52] T. Shinjo, T. Okuno, R. Hassdorf, K. Shigeto, and T. Ono, *Science* 289, 930. 2000.
- [53] R. Antos, Y. Otani, and J. Shibata, *J. Phy. Soc. Jpn.*, vol. 77, 2008.
- [54] Yu. K. Fetisov and C. E. Patton, *IEEE Trans. Magn.* Vol. 40, 473, 2004.
- [55] V. Novosad, M. Grimsditch, K. Y. Guslienko, P. Vavassori, Y. Otani, and S. D. Bader, *Phys. Rev. B.*, vol. 66, 2002.

- [56] H. Zhang, A. Hoffmann, R. Divan, and P. Wang, *Applied Physics Letters.*, vol. 95, 2009.
- [57] V. Novosad, F. Y. Fradin, P. E. Roy, K. S. Buchanan, K. Y. Guslienko, and S. D. Bader, *Phys. Rev. B.*, vol. 72, 024455, 2005.
- [58] A. Vogel, A. Drews, T. Kamionka, M. Bolte, and G. Meier, *Phys. Rev. Lett.*, vol. 105, 037201, 2010.
- [59] K. S. Buchanan, M. Grimsditch, F. Y. Fradin, S. D. Bader, and V. Novosad, *Phys. Rev. Lett.*, vol. 99, 267201, 2007.
- [60] S. Kasai, Y. Nakatani, K. Kobayahi, H. Kohno, and T. Ono, *Phys. Rev. Lett.*, vol. 97, 107204, 2006.
- [61] W. Lin, J. Cucchiara, C. Berthelot, T. Hauet, Y. Henry, J. A. Katine, E. E. Fullerton, and S. Mangin, *Applied Physics Letters.*, vol. 96, 252503, 2010.
- [62] N. Mecking, Y. S. Gui, and C.-M. Hu, *Phys. Rev. B.*, vol. 76, 224430, 2007.
- [63] U. Queitsch, J. McCord, A. Neudert, R. Schafer, L. Schultz, K. Rott, and H. Bruckl, *J. Appl. Phys.*, vol. 100, 093911, 2006.
- [64] I. Neudecker, K. Perzlmaier, F. Hoffman, G. Woltersdorf, M. Buess, D. Weiss, and C. H. Back, *Phys. Rev. B.*, vol. 73, 134426, 2006.